A Computational Investigation of Magnetic Nanoparticle induced Hyperthermia using the Finite Volume Method

A Dissertation Submitted
in partial fulfilment of the requirements
for the degree of

Master of Engineering
in
Thermal Engineering

by

Gurmeet Singh
Registration No.: 801683012

Under the supervision of

Dr. Neeraj Kumar
Assistant Professor

MECHANICAL ENGINEERING DEPARTMENT

THAPAR INSTITUTE OF ENGINEERING & TECHNOLOGY, PATIALA

July, 2018

CERTIFICATE

I hereby declare that the thesis entitled, **"A Computational Investigation of Magnetic Nanoparticle induced Hyperthermia using the Finite Volume Method"** is an authentic record of my work carried out as per requirements for the award of degree of **Master of Engineering** in **Thermal Engineering** at **Thapar Institute of Engineering & Technology, Patiala** under the supervision of **Dr. Neeraj Kumar**, Assistant Professor, Mechanical Engineering Department, Thapar Institute of Engineering & Technology, Patiala during June 2016 to June 2018. No part of the matter embodied in this report has been submitted to any other university or institute for the award of any other degree.

Gurmeet Singh

Date: 21/08/2018

Gurmeet Singh

It is certified that the above statement made by the student is correct to the best of my knowledge and belief.

Dr. Neeraj Kumar
Assistant Professor
Mechanical Engineering Department
Thapar Institute of Engineering & Technology
Patiala-147004

Acknowledgements

I would like to express my sincere gratitude to my supervisor **Dr. Neeraj Kumar, Assistant Professor, Mechanical Engineering Department, TIET, Patiala**, for his continuous encouragement and support of my research. I am grateful to him for believing in my efforts. There were times when things seemed impossible, but with extreme patience and perseverance, he guided me through. I am thankful to him for introducing me to the world of computational analysis.

I would like to thank **Dr. Pramod Kumar Avti, Assistant Professor, Department of Biophysics, PGIMER, Chandigarh**, for providing his valuable suggestions during my research.

I would like to thank **Dr. Vineet Srivastava, Assistant Professor, Mechanical Engineering Department, TIET, Patiala**, for allowing me to use the computational facilities at his lab.

I would also like to express my gratitude to **Rishabh P. Sharma**, for helping me learn how to program algorithms, during the initial phase of my research.

Additionally, I would like to thank the generous people who supported me when I was at my worst, helpless, and hopeless. I am grateful to them for showing continuous faith in me and my efforts.

Gurmeet Singh

Gurmeet Singh

Abstract

In this work magnetic nanoparticle induced hyperthermia has been computationally analyzed using the finite volume method. This work is focused on analysis of variation in treatment parameters (frequency and amplitude of alternating magnetic field, and dose of magnetic nanoparticles injected). The frequency and amplitude values considered for analysis are in accordance with the safe range mentioned in literature. The analysis has been carried out for uniform as well as nonuniform spatial distribution of intratumorally injected magnetic nanoparticles. Gaussian distribution has been used to model nonuniform distribution of magnetic nanoparticles. Nonuniform distribution of magnetic nanoparticles has been used for cases of single-point as well as multi-point injection. Magnetite nanoparticles have been considered for analysis.

Computation has been carried out for one-dimensional, two-dimensional, and three-dimensional geometric models. For the one-dimensional model that consists of only healthy tissues, numerical solutions have been obtained for time dependent as well as steady state cases. Results for both cases have been validated with the analytical solutions. The two-dimensional model, consisting of a tumor surrounded by healthy tissues, has also been analyzed for steady as well as time dependent cases. The results obtained using finite volume method agree well with those reported in literature, using lattice Boltzmann method, and finite element method.

Variation in amplitude of the alternating magnetic field is initially analyzed on the three-dimensional model, which also consists of a tumor surrounded by healthy tissues. 5 $kA.m^{-1}$, 7.5 $kA.m^{-1}$, and 10 $kA.m^{-1}$, are the values of amplitude that were considered in analysis. Results revealed that with increment in magnetic field amplitude, temperature within the tumor also increases. Similar results were obtained when frequency values of, 50 kHz, 75 kHz, and 100 kHz, were used. Highest increments in temperature were observed for single point injection, and lowest with uniform distribution, with increase in both amplitude and frequency of the magnetic field. It was also observed that with multi-point injection a more uniform temperature distribution is obtained, in contrast to single-point injection and uniform distribution of nanoparticles. Variation in nanoparticle dose is analyzed using the values, 4 mg of magnetite / cm^3 of tumor, 5 mg of magnetite / cm^3 of tumor, and 6 mg of magnetite /cm^3 of tumor. Results reveal that increments in nanoparticle dose also result in increase in temperature.

Greater variation in temperature is observed with variation in treatment parameters if the injected nanoparticle mass at a specific location is also high. Temperature variation is more pronounced with variation in amplitude and frequency, than it is with nanoparticle dose.

Contents

List of Figures

List of Tables

Nomenclature

Parameters	**Description**
ρ_t	Tissue Density
c_{pt}	Specific heat of the tissue
T	Temperature
t	Time
k_t	Thermal conductivity of the tissue
η_b	Perfusion rate of blood
ρ_b	Density of blood
c_{pb}	Specific heat of blood
T_a	Arterial blood temperature
Q_m	Metabolic heat generation rate
Q_s	Heat generation rate due to an external source
μ_0	Permeability of free space
χ_0	Chord susceptibility
H_0	Amplitude of the alternating magnetic field
f	Frequency of the alternating magnetic field
τ	Effective relaxation time
τ_B	Brownian relaxation time
τ_N	Néelian relaxation time
η	Dynamic viscosity of the fluid carrying magnetic nanoparticles
V_H	Hydrodynamic volume of magnetic nanoparticle
k_b	Boltzmann constant

ϕ	Volume fraction of magnetic nanoparticles
M_d	Domain magnetization
V_M	Volume of magnetic nanoparticle core
τ_0	Attempt time
χ_i	Initial susceptibility
K	Magneto crystalline anisotropy constant
R	Radius of magnetic nanoparticle
δ	Ligand thickness
g	Distribution function
$\sigma_x, \sigma_y, \sigma_z$	Standard deviation along the x, y, and z direction
$\overline{x}, \overline{y}, \overline{z}$	Mean along the x, y, and z direction
α	Thermal diffusivity

Abbreviations

Abbreviations	Definition
AMF	Alternating Magnetic Field
MNPs	Magnetic Nanoparticles
SAR	Specific Absorption Rate
LBM	Lattice Boltzmann Method
GNRs	Gold Nanorods
BVs	Blood Vessels
LCT	Low Curie Temperature
HCT	High Curie Temperature
PBHTE	Pennes' Bioheat Transfer Equation
FDM	Finite Difference Method
FVM	Finite Volume Method
FEM	Finite Element Method
RMSE	Root Mean Square Error
TL	Therapeutic Limit
TB	Tumor Boundary

Chapter 1

Introduction

Millions of people lose their lives to cancer every year. According to the World Health Organization, cancer is the second highest cause of death worldwide [1].

One might ask, what makes it so lethal? Cancer becomes lethal when tumors become so large that they hinder the functionality of healthy cells surrounding them. Not all tumors exhibit this behavior. Some of them are benign as well. The tumors that are benign, grow up to a certain extent, after which their growth ceases. This is due to restrictions in growth space. In case of malignant tumors, growth never ceases. As they grow in size, so does their need for nutrients and oxygenated blood. This results in growth of vasculature networks, that supply blood to the tumor. With blood flowing through the tumor, there are times when tumor cells escape into the blood stream and reach different parts of the body. These cells then grow into secondary tumors, exhibiting the same lethal behavior as the parent tumor. This uncontrolled growth of tumors, if not treated, proves fatal for the patient.

Various cancer treatment techniques are available today. Some of them have been in use for a very long time (surgery, chemotherapy, and radiotherapy), and some have just emerged in the last few decades (immunotherapy, targeted therapy, and hormonal therapy). Most of the time, two or more of these treatments are used in conjunction. Surgery is usually preferred first, to remove as much mass of the tumor as possible. With surgery, complete removal of tumor is not always possible, therefore other techniques are used post-surgery, to shrink the tumor mass left behind, and eventually kill the cells that can cause tumor recurrence [2].

The process of treating cancer is not always so straightforward, as the treatment techniques mentioned above have certain harmful long-term aftereffects associated with them. Some of them are, lymphedema, infertility, congestive heart failure, coronary artery disease, arrythmia, hypertension, lung damage, hormonal imbalance, cognitive problems, and tumor recurrence [3]. In some cases, patients have to undergo treatments for years, in order to prevent tumor recurrence. Such people develop life threatening diseases with age, due to the treatment they underwent. Therefore, the lives of cancer patients as well as cancer survivors have become extremely difficult, due to the disease itself, and aftereffects of the techniques used to treat it. The world needs an alternative to the current cancer treatment techniques, and this alternative should neither be invasive, nor should it have any harmful long-term aftereffects. Today, heat is being used as that alternative.

In ancient times, heat was used to treat various physical ailments [4]. Until the year 1883, a lot of people did not know about the effects of heat on tumors. In 1883, in a work presented by Fehleisen, the dependency between tumor growth rate and body temperature was first brought forth [5]. He induced erysipelas in patients suffering from cancer and discovered that due to the

fever caused by erysipelas, the tumors in some patients decreased to half of their original size, and in others they completely disappeared. W. B. Coley continued this by carrying out similar experiments on patients who were suffering with malignant diseases [6]. His observations were similar to those of Fehleisen. He even stated that the chances of survival of a patient depended on the degree of intensity of the fever induced in the patient, the more intense the fever, greater are the chances of patient survival. Initially it was believed that tumor regression was due to high body temperatures only, but later it was discovered that the immunological responses of a patient's body cause this. The human body at
the immune system agitated due to high body temperature, it is able to do so. The immunological responses of the body initiate cell apoptosis within the tumor. Hence, a reduction in tumor size, and an eventual disappearance is observed with high body temperature.

During the 1900s, this practice of usage of high body temperatures to treat cancer began to be called as thermotherapy or hyperthermia treatment. During hyperthermia, the tumor is usually kept above 42-43^{o}C (therapeutic limit), while the healthy tissues surrounding it, below this limit. Even after producing promising results, hyperthermia remained in negligence, and was overshadowed for more than 50 years by the conventional treatment techniques. However, today it is being looked upon as a replacement for all current cancer treatment techniques. This is due to its aftereffects, that are less intense and temporary, in contrast to those of the current treatment techniques.

The mode of inducing hyperthermia depends on the diseased region. In case of cancer metastasis, whole body hyperthermia is used. Generally hot water baths are used for this. If only a limb or organ is affected by the disease, then regional hyperthermia is used, in which blood perfusing through the affected region is extracted, heated, and then reintroduced into the body through the affected region. If a tumor has to be directly targeted, then local hyperthermia is used. For this, metallic seeds and probes were used. They were surgically placed in close proximity of the tumor, or within it, and were then heated with external sources or an alternating magnetic field (AMF). It was later discovered that the heat distribution due to these probes and seeds was nonuniform, as heat concentration regions developed where they were placed. Therefore, only those cells were affected by the treatment that were in vicinity of the probes and seeds, the cells that were distant from them remained unaffected [7]. It is due to this reason that they were later replaced by magnetic nanoparticles (MNPs).

MNPs offer several advantages over other methods of inducing localized hyperthermia. They do not require invasive procedures for introduction within the body, instead they can just be injected. Being small in size aids them to spread in a more uniform manner, thus providing better heat distribution than what was obtained with metallic seeds and probes. They offer selective heating, i.e. heating only the region where they are injected, unlike other methods that also heated the healthy tissues surrounding a tumor. Clinical trials of MNP induced hyperthermia on humans, have already begun [8].

To induce localized hyperthermia MNPs are either injected intravenously, or intratumorally. In intravenous injection, MNPs are injected into the veins that carry blood to the tumor, whereas in intratumoral injection, they are injected directly into the tumor. Under the influence of an AMF, they dissipate heat. MNPs are usually injected intratumorally when tumors are not deep seated. In order to produce best outcomes, the optimum dose of MNPs to be injected, as well as the locations that they should be injected at must be known before treatment initiation. Along with these, the values of parameters that affect the AMF behavior (i.e. frequency, and amplitude of the field), must also be known beforehand. This can be done only by simulating the treatment, before it is actually performed. Simulation of the treatment requires computational analysis of the mathematical equations governing the physical phenomena that occurs during the treatment.

In this work, computational analysis of hyperthermia treatment is performed, using the finite volume method. This work is focused on, analysis of variations in treatment parameters (frequency and amplitude of AMF, and the MNP dose injected) when intratumorally injected MNPs are uniformly, and nonuniformly spatially distributed. Nonuniform spatial distribution is considered for cases of single as well as multiple intratumoral injections.

1.1 Background

All mammals and birds have an adaptive immune system, which protects them against all foreign bodies. Anything that the human body considers foreign is removed from it. The reticuloendothelial system aids in doing so. Right after the MNPs are injected, either intravenously, or intratumorally, they are adsorbed by the plasma proteins, called opsonins. On reaching the liver, kidneys, and spleen, along with the bloodstream, they are caught by the phagocytic cells of the reticuloendothelial system and are then removed from the body in the form of excrement [9]. The only way to ensure that the MNPs are not adsorbed by the opsonins, is to coat them with a biocompatible material. The biocompatible coating aids in camouflaging the MNPs from the immune system. The coating is so designed that it allows the MNPs to remain undetected for the desired therapeutic time. After treatment completion, the immune system removes them from the body. Dextran, and PEG are generally used to make such coatings [9]. In various in-vivo studies it was observed that MNPs which have a larger hydrodynamic diameter, tend to get caught sooner by the opsonins [9]. Therefore, the hydrodynamic diameter of a MNP should be such that the particle can remain undetected at the desired location within the body for given therapeutic time.

Generally, single domain MNPs, whose hydrodynamic diameters are less than 100 nm, are used in hyperthermia. Heat generation in particles of such small size occurs only due to relaxation mechanisms, viz. Néelian, and Brownian relaxation mechanisms [10]. Brownian relaxation occurs when a MNP, under the influence of an AMF, experiences magnetic dipole reversal with respect to its surrounding fluid. This leads to heat generation due to shearing between the MNP and its surrounding fluid. Néelian relaxation is observed when magnetic dipole reversal of the MNP occurs with respect to its crystal structure. Out of the two, whichever relaxation mechanism takes minimum time, is the more dominating one for heat generation.

The parameters that have been observed to affect the temperature distribution during hyperthermia treatment are, the hydrodynamic diameter of the particle, the MNP dose to be injected, amplitude and frequency of the applied field, and spatial distribution patterns of MNPs.

1.2 Literature Survey

Various studies associated with experimental as well as computational analysis of MNP induced hyperthermia have been reported in literature. All such studies are described below, in respective sections:

1.2.1 *Experimental studies*

1. ***Hilger et al.*** [11]**,** in 2001, presented an analysis of the effects of MNP dose on temperature elevation within breast tissues. They also analyzed the effects of treatment parameters on immunodeficient rats bearing adenocarcinomas. Their observations in breast tissue revealed that temperature elevation is a linear function of injected MNP mass. With increase in injected MNP mass, the temperature within the tissue increases. This behavior is observed only up to a specific value of MNP mass, above which there is no effect on tissue temperature. Shrinkage of tumors in mice after heating was also observed.

2. ***Johannsen et al.*** [12], conducted experiments on tumor bearing Copenhagen rats, to compare the effects on tumor growth, when radiotherapy alone is used, versus when MNP induced hyperthermia is used in conjunction with radiotherapy. Their observations revealed that tumor regression is possible with considerably less doses of radiation when hyperthermia is used with radiotherapy. They stated that a radiation dose of 20 Gy with hyperthermia, has the same effect on tumor growth, as 60 Gy of radiation alone.

3. ***Salloum et al.*** [13], discussed the effects of infusion rates on MNP spread in MNP induced hyperthermia. They conducted experiments on agarose gel. Their observations revealed that MNPs after intratumoral injection are not uniformly distributed in space, rather they follow Gaussian distribution. This was revealed when the specific absorption rate (SAR) pattern was analyzed. High temperature was observed at the injection site and in its proximity. They also stated that infusion rates of MNPs have a significant effect on the extent of their spread. They stated that slow MNP infusion rates are required in order to obtain a spatial distribution pattern that approximates Gaussian distribution.

1.2.2 *Computational studies*

1. ***S. Maenosono*** and ***S. Saita*** [14], in their study conducted an in-vitro comparitive study of, magnetite, maghemite, FeCo, fcc FePt, and $L1_0$ FePt MNPs. They have used aqueous dispersions of particles to compare their heating rates, at different frequencies and amplitudes of the AMF. They discovered that fcc FePt MNPs have a superior heating capability in

comparison to the other MNPs used in the study. They have also analyzed the same computationally and found good agreement between the experimental and computational observations.

2. ***H. Zhang*** [15], conducted a computational study of hyperthermia using the Lattice Boltzmann method (LBM). The sole purpose behind this study was to check the applicability of LBM in studies associated with hyperthermia. He conducted the analysis on one-dimensional and two-dimensional geometric models, for time dependent as well as steady state cases. His work affirmed the applicability of LBM in analysis of hyperthermia.

3. In another study presented by ***Salloum et al.*** [16], an optimization algorithm was developed to evaluate the optimum heat distribution pattern due to multiple intratumoral MNP injection sites. The optimization was based on keeping the temperature within 90% of the tumor and only 10% of the healthy tissues surrounding it, close to the therapeutic limit (43^{o}C). They have used injection site locations, thermo-physical properties of the tumor and healthy tissues, and their respective blood perfusion rates as the algorithm inputs. Their analysis was conducted on Comsol Multiphysics.

4. ***A. A. Golneshan*** and ***M. Lahonian*** [17], presented a study in which they have computationally analyzed MNP induced hyperthermia in a three-dimensional geometry, using LBM. The geometry that they had considered consists of two concentric spheres, the inner sphere depicting a tumor, while the outer depicting the nearby healthy tissues. They have compared the effects of SAR distribution (homogenous and Gaussian distribution) on temperature distribution within the study domain.

5. ***M. Lahonian*** and ***A. A. Golneshan*** [18], through another study presented the effects of several treatment parameters on temperature distribution within a tumor and the healthy tissues in its vicinity. They have conducted the analysis on the same geometric model that they had considered in their last study. The parameters which were analyzed are, magnetic induction, frequency and amplitude of AMF, volume fraction of MNPs, and blood perfusion rates. They have also presented effects of MNP spatial distribution patterns (homogenous, parabolic, and linear distribution) on temperature distribution within the study domain.

6. In another study, ***A. A. Golneshan*** and ***M. Lahonian*** [19], have analyzed the effects of multiple MNP injection sites on temperature distribution in MNP induced hyperthermia using LBM. Their analysis was conducted on one-dimensional and two-dimensional models. They have also analyzed the effects of injection volume, and infusion flow rates. Results revealed that temperature distribution within the study domain is more uniform with multi point injection in comparison to single point injection. Their results also revealed that high MNP infusion rates cause MNPs to accumulate near the injection site, therefore complete tumor does not receive adequate heat.

7. ***M. Mital*** and ***H. V. Tafreshi*** [20], in their study have conducted computational analysis of MNP induced hyperthermia to optimize the treatment parameters, using a genetic algorithm. The geometric model that they have used is similar to what ***Lahonian*** and ***Golneshan*** [18] had used, two concentric spheres, the inner depicting a tumor, and the outer, nearby healthy tissues. They have considered Gaussian distribution of SAR, that decays exponentially in time. Thermal damage within the tumor was also evaluated. The analysis was carried out on Comsol.

8. ***Soni et al.*** [21], in their study have analyzed the effects of spatial distribution patterns of gold nanorods (GNRs) on temperature distribution. Their study was focused on attainment of thermo-ablative temperatures within the tumor (50-60^{o}C). They have conducted the analysis on a two-dimensional model, consisting of two concentric cylinders, the inner depicting a tumor, and the outer, healthy tissues. They have carried out the analysis for, uniformly distributed GNRs within the tumor, GNRs accumulated at tumor center (a case of intratumoral GNR injection), and GNRs distributed in tumor periphery (a case of intravenous GNR injection). Favorable results were obtained with GNRs distributed in tumor periphery.

9. ***Astefanoaei et al.*** [22] in their study have conducted computational analysis of hyperthermia in a three-dimensional geometric model. Their model depicts a spherical tumor embedded in cubical domain of healthy tissues, with blood vessels passing through the tumor. They have compared three MNPs in their study, viz. FeCrBNb, maghemite, and magnetite MNPs. Their study illustrates the effects that number of blood vessels, concentration of MNPs at injection sites, blood vessel diameter, and the blood velocity have on temperature distribution within the study domain. Their analysis was carried out on Comsol Multiphysics.

10. ***Yue et al.*** [23] have analyzed the effects of blood flowing through bifurcated blood vessels (BVs) on temperature distribution, during MNP induced hyperthermia. The geometric model on which their analysis was carried out consisted of an irregular shaped tumor that approximated a sphere, located within a cubical domain of healthy tissues. Bifurcated BVs were assumed to be passing through the tumor. MNPs were assumed to be diffusing from the injection sites. Their study sheds light upon the effects that size and position of bifurcated BVs, have on heat and mass transfer of MNPs. They have stated that a large number of injection sites with high MNP concentration are required to minimize the heat sink effect of blood vessels.

11. ***Soetaert et al.*** [24], through their study have illustrated the effects of amplitude modulations of AMF on temperature distribution in MNP induced hyperthermia. They have carried out the analysis on a three-dimensional geometry that depicts a tumor surrounded by healthy tissues. MNP mass distribution within the tumor is considered to be Gaussian. Thermal damage of tissues based on temperature has also been evaluated. They have assumed thermal damage dependent blood perfusion in their analysis. They have also shown the effects of spread of MNPs within the tumor.

12. Another work presented by ***Soetaert et al.*** [25], illustrates the effects of polydisperse spatial distribution of maghemite and magnetite MNPs on temperature distribution. They have also illustrated the effects of, extent of MNP spatial distribution, on temperature distribution.
13. ***Tang et al.*** have demonstrated the advantages of low Curie temperature (LCT) MNPs over MNPs with high Curie temperatures (HCT) used in MNP induced hyperthermia. They have computationally analyzed the treatment in a model of liver. Presence of blood vessels, and nanoparticle clustering after injection have also been considered in their analysis. Their results revealed that MNPs with LCT have a better therapeutic effect than the standard magnetite MNPs.

1.3 Gaps Identified

1. Most of the computational studies conducted have considered distribution of the SAR, rather than the distribution of MNP mass. In reality it is the injected MNPs that are distributed, which most of the studies done so far fail to address.
2. Almost all of the studies have been carried out for deep seated tumors, and therefore fail to consider the effects of heat loss to the surroundings during treatment
3. Most studies have been for MNPs injected at a single site within the tumor. It has been observed in experimental studies that single site injection of MNPs fails to maintain the complete tumor above the therapeutic limit.
4. Most studies have also failed to address the effects of the extent of MNP spread on temperature distribution. It has been reported in experimental studies that the spread of MNPs after injection in a tissue, depends on the viscosity of the MNP carrying medium, injection rate, and density of the tissue. All these can greatly affect the temperature distribution within the tumor and its surrounding tissues during treatment.
5. The computational studies associated with multi-site MNP injections, have been for one-dimensional and two-dimensional models. Such studies therefore fail to present the realistic effects of treatment parameters and conditions.
6. Most studies have not addressed the differences between the temperature distribution observed during single-site and multi-site MNP injection.

1.4 Objectives of the present work

1. To study the effects of treatment parameters (amplitude and frequency of the AMF, and dose of MNPs injected) on temperature distribution.

2. To compare the uniform (ideal case) and nonuniform (single-point and multi-point injection of MNPs) spatial distribution patterns of MNPs.
3. Based on outcomes of the analysis, prediction of the spatial distribution pattern that is effective as well as efficient.

1.5 Thesis outline

Chapter 2 introduces the reader to the governing equations that are used in analysis. One of those equations, called the Pennes' bioheat (PBHTE) governs the transfer of heat through biological tissues. The rest of the relations govern the process of heat dissipation of MNPs. This chapter also introduces the reader to FVM, its discretization process, and how the Dirichlet, Neumann, and Robin boundary conditions are applied. Additionally, a relation that was used to model nonuniform spatial distribution of MNPs is also presented at the end of this chapter.

Chapter 3 introduces the reader to a comparative study performed by the author, that validates the applicability of FVM. This chapter begins with introduction to a one-dimensional model of healthy tissues, in which temperature distribution is evaluated when, the model is not time dependent, and when it is. In subsequent sections, a similar analysis is carried out on a two-dimensional model that depicts a tumor surrounded by healthy tissues.

In chapter 4, objectives stated in the prior section are addressed. Three different spatial distribution patterns of MNPs are considered for analysis, viz., uniform distribution, and nonuniform distribution when MNPs are injected at single and multiple sites. First section of this chapter introduces the reader to a grid independent test, which was performed to check the accuracy of the numerical solution. In the sections subsequent to it, temperature distributions due to varying treatment parameters (frequency and amplitude of AMF, and MNP dose), for all cases of MNP spatial distribution patterns are presented. Based on the results, the efficacy and efficiency of these spatial distribution patterns is discussed.

Chapter 5 includes conclusions based on the results obtained in chapter 4. This chapter also addresses the improvements that can be made in this study, in order to enhance its validity.

Chapter 2

Mathematical Modeling

2.1 Pennes' bioheat transfer equation

Today, there are various mathematical relations available, that can be used to model the transfer of heat in biological tissues. Out of all such relations, PBHTE [27], has been used the most in studies associated with bioheat transfer. This is due to its simple mathematical nature, and the high accuracy with which it is able to predict the temperature [28]. It is generally used for tissues that are devoid of major blood vessels, and only contain beds of minute capillaries. The time dependent form of PBHTE is given below,

$$\rho_t c_{pt} \frac{\partial T}{\partial t} = \nabla k_t \nabla T + \eta_b \rho_b c_{pb} (T_a - T) + Q_m + Q_s \tag{1}$$

Here, ρ_t, c_{pt}, and k_t represent the density (kg.m^{-3}), specific heat (J.kg^{-1}.K^{-1}), and thermal conductivity of the tissue (W.m^{-1}.K^{-1}), respectively, T represents the temperature (K), t the time (s), Q_m the metabolic heat generation rate (W.m^{-3}), and Q_s the heat dissipation rate due to an external source (W.m^{-3}), T_a the arterial blood temperature (K), and ρ_b, c_{pb}, η_b the density (kg.m^{-3}), specific heat (J.kg^{-1}.K^{-1}), and perfusion rate of the blood (s^{-1}).

2.2 Heat dissipation due to MNPs

As stated in section 1.1, heat generation in MNPs occurs through combination, or individualistic domination of the relaxation mechanisms, viz. Néelian and Brownian relaxation mechanisms. This dominance is dependent on the time for which each relaxation mechanism occurs. Out of the two, whichever mechanism takes lesser time, becomes dominant [29]. This behavior has also been observed to be MNP diameter dependent [10].

Heat dissipation of MNPs during hyperthermia also depends on, amplitude and frequency of the AMF, MNP dose, MNP diameter and thickness of the biocompatible coating used, and viscosity of the MNP carrier fluid.

The relations for heat dissipation of spherical monodispersed MNPs are given as [29],

$$P = \pi \mu_0 \chi_0 H_0^2 f \frac{2\pi f \tau}{1 + (2\pi f \tau)^2} \tag{2}$$

$$\chi_0 = \chi_i \frac{3}{\xi} \left(\coth \xi - \frac{1}{\xi} \right) \tag{3}$$

$$\frac{1}{\tau} = \frac{1}{\tau_B}+\frac{1}{\tau_N} \tag{4}$$

$$\tau_B = \frac{3\eta V_H}{k_b T} \tag{5}$$

$$\tau_N = \frac{\sqrt{\pi}}{2}\tau_0 \frac{\exp\Gamma}{\Gamma^{1/2}} \tag{6}$$

$$\chi_i = \frac{\mu_0 \phi M_d^2 V_M}{3k_b T} \tag{7}$$

$$\xi = \frac{\mu_0 M_d H V_M}{k_b T} \tag{8}$$

$$V_H = \frac{4}{3}\pi(R+\delta)^3, \qquad V_M = \frac{4}{3}\pi R^3, \qquad \Gamma = \frac{K V_M}{k_b T}, \qquad H = H_0 \cos 2\pi f t.$$

Here, P is the heat dissipation rate of MNPs (W.m^{-3}), μ_0 is the permeability of free space $4\pi\times10^{-7}$ (T.m.A^{-1}) [30], χ_0 is the chord susceptibility, H_0 is the amplitude of AMF (A.m^{-1}), f is the frequency of AMF (Hz), τ is the effective relaxation time (s), χ_i is the initial susceptibility, τ_B is the Brownian relaxation time (s), τ_N is the Néelian relaxation time (s), η is the viscosity of carrier fluid (N.s.m^{-2}), V_H is the hydrodynamic volume of the MNP (m^3), k_b is the Boltzmann constant 1.38×10^{-23} (J.K^{-1}) [30], τ_0 is the attempt time 10^{-9} (s) [30], ϕ is the volume fraction of MNPs, M_d is the domain magnetization (A.m^{-1}), V_M is the volume of MNP (m^3), R is the radius of MNP (m), δ is the thickness of biocompatible coating over the MNP core (m), and K is the magneto-crystalline anisotropy constant (J.m^{-3}).

2.3 The finite volume method

Solving equations such as (1) over a domain with given boundary and initial conditions is a difficult task. Usually, such partial differential equations are solved with the help of numerical methods. Numerical methods require dividing the main study domain into multiple minute sub-domains, as the physical behavior of the equation can be approximated only in very small regions. If tried for the whole domain at once, this procedure will lead to an erroneous solution. These sub-domains can be quadrilaterals or triangles, if the main domain is two-dimensional, or tetrahedrons, pyramids, and hexahedrons, in case it is three-dimensional. The equation is then solved over these sub-domains to evaluate the dependent variable in the equation. The evaluated values are location specific. These locations can be either, the sub-domain vertices, or their centers.

FVM is used in this study because it has some advantages over other numerical methods. The basic philosophy on which it is based is conserving the nature of the equation, over the sub-domains, as well as the main domain. This means that it ensures that the conservational law on which an equation is based, is obeyed within the sub domains as well as the main domain [31]. Other numerical methods do not follow this philosophy, e.g. the finite difference method (FDM), in which only the mathematical formulations of the equations are considered important, not the conservational law which an equation governs. Being computationally less expensive than other numerical methods is also one of the reasons why it is more preferred. FVM is preferred for problems that require analysis of fluid flow, which may include mass, momentum, and energy transfer. This serves as another reason for the choice of FVM in this study.

2.3.1 *Derivation of equations for the discretized sub-domains*

The process of dividing the main study domain into minute sub-domains is called discretization. These sub-domains are called finite volumes or control volumes. The value of the dependent variable of an equation is stored at the center of a control volume. A control volume has faces that bound it and are shared by its neighbors. The neighbors of a control volume on its eastern, western, northern, and southern sides, are generally denoted by *E*, *W*, *N*, and *S*. Similarly, the faces it shares with them, are denoted by, *e*, *w*, *n*, and *s*. The distance between centers of two control volumes along the x-axis and y-axis, is denoted by Δx, and Δy,

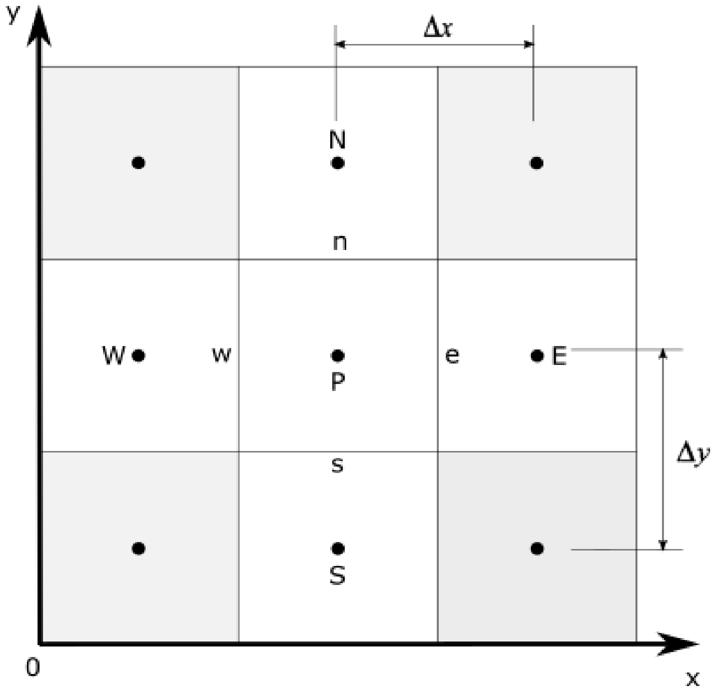

Fig. 2.1. A general control volume, along with its neighbors.

respectively. A two-dimensional quadrilateral (rectangular) control volume, *P*, along with its neighbors, is shown in *Fig. 2.1*.

In FVM, the discretized form of a governing equation for a specific control volume is obtained by integrating it over its volume. If the equation is time dependent, it must also be integrated over time. The lower limit for integration over time is taken as *t*, and the upper limit as *t*+1. Therefore, the discretized form of equation (1), for two cartesian spatial dimensions, is derived as,

$$\begin{aligned}\int_t^{t+1}\int_s^n\int_w^e \rho_t c_{pt}\frac{\partial T}{\partial t}\,dx\,dy\,dt \quad &= \quad \int_t^{t+1}\int_s^n\int_w^e \frac{\partial}{\partial x}\left(k_t\frac{\partial T}{\partial x}\right)dx\,dy\,dt \\ &+ \quad \int_t^{t+1}\int_s^n\int_w^e \frac{\partial}{\partial y}\left(k_t\frac{\partial T}{\partial y}\right)dx\,dy\,dt \\ &+ \quad \int_t^{t+1}\int_s^n\int_w^e \eta_b\rho_b c_{pb}(T_a - T)\,dx\,dy\,dt \\ &+ \quad \int_t^{t+1}\int_s^n\int_w^e (Q_m + Q_s)\,dx\,dy\,dt \qquad (9)\end{aligned}$$

The terms on right side of equation (9), after integration become,

$$\begin{aligned}\int_{\mathrm{t}}^{t+1}\int_s^n\int_w^e \rho_t c_{pt}\frac{\partial T}{\partial t}\,dx\,dy\,dt \quad &= \quad \int_t^{t+1}\left[\left(k_{tx}\frac{\partial T}{\partial x}\right)_e - \left(k_{tx}\frac{\partial T}{\partial x}\right)_w\right]\Delta y\,dt \\ &+ \quad \int_t^{t+1}\left[\left(k_{ty}\frac{\partial T}{\partial y}\right)_n - \left(k_{ty}\frac{\partial T}{\partial y}\right)_s\right]\Delta x\,dt \\ &+ \quad \int_t^{t+1}\left[\eta_b\rho_b c_{pb}(T_a - T)\Delta x\,\Delta y\right]dt \\ &+ \quad \int_t^{t+1}\left[(Q_m + Q_s)\Delta x\,\Delta y\right]dt \qquad (10)\end{aligned}$$

The term on left side of equation (10), can be written as,

$$\int_t^{t+1}\int_s^n\int_w^e \rho_t c_{pt}\frac{\partial T}{\partial t}\,dx\,dy\,dt \quad = \quad \int_s^n\int_w^e\int_t^{t+1} \rho_t c_{pt}\frac{\partial T}{\partial t}\,dt\,dx\,dy$$

After integrating the above relation with respect to time, it becomes,

$$\int_s^n\int_w^e \rho_t c_{pt}(T_P^{t+1} - T_P^t)dx\,dy$$

Which, after spatial integration becomes,

$$\rho_t c_{pt}(T_P^{t+1} - T_P^t)\Delta x\,\Delta y \qquad (11)$$

The terms on right side of equation (10) containing thermal conductivities, can be written as,

$$\left(k_{tx}\frac{\partial T}{\partial x}\right)_e = k_{txe}\left.\frac{\partial T}{\partial x}\right|_e \tag{12}$$

$$\left(k_{tx}\frac{\partial T}{\partial x}\right)_w = k_{txw}\left.\frac{\partial T}{\partial x}\right|_w \tag{13}$$

$$\left(k_{ty}\frac{\partial T}{\partial y}\right)_n = k_{tyn}\left.\frac{\partial T}{\partial y}\right|_n \tag{14}$$

$$\left(k_{ty}\frac{\partial T}{\partial y}\right)_s = k_{tys}\left.\frac{\partial T}{\partial y}\right|_s \tag{15}$$

Thermal conductivities at control volume faces are evaluated as the inverse distance-weighted harmonic mean of the thermal conductivities of control volumes that share those faces.

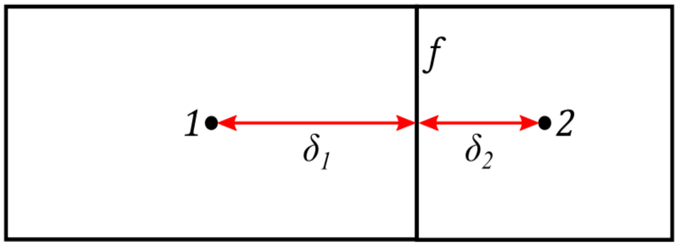

Fig. 2.2. Control volumes 1 and 2, at distances δ_1 and δ_2, from interface f.

Considering *Fig. 2.2*, the inverse distance-weighted harmonic mean of thermal conductivities of control volumes 1, and 2, is calculated from the relation [31],

$$k_f = \frac{k_1 k_2}{\frac{k_1\delta_2 + k_2\delta_1}{\delta_1 + \delta_2}} \tag{16}$$

Here, k_f is the thermal conductivity of the face f, k_1 and k_2 are the thermal conductivities of control volumes 1 and 2, the centers of which are located at distances δ_1, and δ_2 from face f, respectively.

If k_P, k_E, k_W, k_N, and k_S, are thermal conductivities of control volumes P, E, W, N, and S, and are all equal to k, then with the help of equation (16), the thermal conductivities of respective control volume faces can be obtained as,

$$k_{txe} = k_{txw} = k_{tyn} = k_{tys} = k \tag{17}$$

The temperature gradients at control volume faces in equations (12), (13), (14), and (15) can be approximated with Taylor series expansions. For face e, the relation would become,

$$
\begin{aligned}
T_E &= T_e + \frac{\Delta x}{2}\frac{\partial T}{\partial x}\bigg|_e + \frac{1}{2}\left(\frac{\Delta x}{2}\right)^2 \frac{\partial^2 T}{\partial x^2}\bigg|_e \\
&+ \frac{1}{6}\left(\frac{\Delta x}{2}\right)^3 \frac{\partial^3 T}{\partial x^3}\bigg|_e + \cdots \qquad (18) \\
T_P &= T_e - \frac{\Delta x}{2}\frac{\partial T}{\partial x}\bigg|_e + \frac{1}{2}\left(\frac{\Delta x}{2}\right)^2 \frac{\partial^2 T}{\partial x^2}\bigg|_e \\
&- \frac{1}{6}\left(\frac{\Delta x}{2}\right)^3 \frac{\partial^3 T}{\partial x^3}\bigg|_e + \cdots \qquad (19)
\end{aligned}
$$

From equations (18), and (19), the following relation for temperature gradient at face e is obtained,

$$
\frac{\partial T}{\partial x}\bigg|_e = \frac{T_E - T_P}{\Delta x} - \frac{(\Delta x)^2}{24}\frac{\partial^3 T}{\partial x^3}\bigg|_e + \cdots \qquad (20)
$$

Only the first term on right hand side of equation (20) is used to replace the temperature gradient at face e. Relations for temperature gradients at other faces can be similarly evaluated. On substituting the relations of equations (11), (17), and (20), in equation (10), and using the backward Euler method for temporal integration, the following equation is obtained,

$$
\begin{aligned}
\rho_t c_{pt}(T_P^{t+1} - T_P^t)\,\Delta x\,\Delta y &= k\,\Delta y\left[\left(\frac{T_E^{t+1} - T_P^{t+1}}{\Delta x}\right) - \left(\frac{T_P^{t+1} - T_W^{t+1}}{\Delta x}\right)\right]\Delta t \\
&+ k\,\Delta x\left[\left(\frac{T_N^{t+1} - T_P^{t+1}}{\Delta y}\right) - \left(\frac{T_P^{t+1} - T_S^{t+1}}{\Delta y}\right)\right]\Delta t \\
&+ \eta_b \rho_b c_{pb}(T_a - T_P^{t+1})\,\Delta x\,\Delta y\,\Delta t \\
&+ (Q_m + Q_s)\,\Delta x\,\Delta y\,\Delta \mathrm{t} \qquad (21)
\end{aligned}
$$

Equation (21) after further simplification, can be written as,

$$
\begin{aligned}
(T_P^{t+1} - T_P^t)a_P^o &= kA_x\left[\left(\frac{T_E^{t+1} - T_P^{t+1}}{\Delta x}\right) - \left(\frac{T_P^{t+1} - T_W^{t+1}}{\Delta x}\right)\right] \\
&+ kA_y\left[\left(\frac{T_N^{t+1} - T_P^{t+1}}{\Delta y}\right) - \left(\frac{T_P^{t+1} - T_S^{t+1}}{\Delta y}\right)\right] \\
&+ \eta_b \rho_b c_{pb}(T_a - T_P^{t+1})\,\Delta V \\
&+ (Q_m + Q_s)\,\Delta V \qquad (22)
\end{aligned}
$$

Where,

$$
a_P^o = \frac{\rho_t c_{pt} \Delta V}{\Delta t}
$$

$$A_x = \Delta y$$

$$A_y = \Delta x$$

$$\Delta V = \Delta x \, \Delta y$$

Equation (22) is the discretized form of equation (1). In a similar way it can be extended to consider an extra spatial dimension. Equation (22) can be solved using the Gauss Seidel iterative method.

2.3.2 *Application of boundary conditions*

Generally, three kinds of boundary conditions are encountered in numerical studies. The first one is when the dependent variable of an equation is specified as a constant at the domain boundary. This is called the Dirichlet boundary condition. The second one when the dependent variable is specified in the form of spatial gradient at the domain boundary. This is called the Neumann boundary condition. The third one is when the dependent variable is specified as a combination of Dirichlet, and Neumann boundary conditions, at the domain boundary. This is called the Robin boundary condition. The procedures that should be followed to apply these boundary conditions, are explained in the following sections.

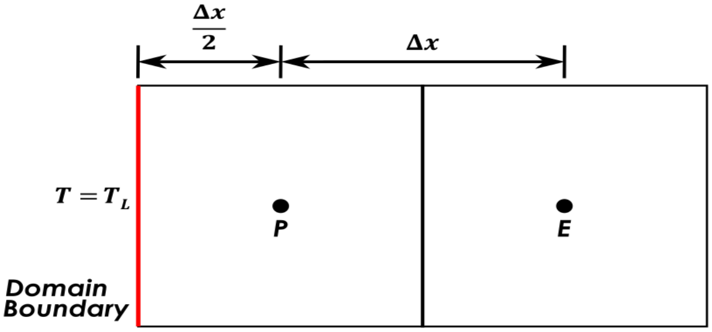

Fig. 2.3. Illustration of the Dirichlet boundary condition.

2.3.2.1 The Dirichlet boundary condition

The Dirichlet boundary condition is illustrated in *Fig. 2.3*. Usually the boundary conditions in FVM that have an order of accuracy greater than one are preferred and are applied to the flux (spatial gradient of the dependent variable) terms. In order to apply the Dirichlet boundary condition on western face of the control volume *P*, shown in *Fig. 2.3*, Taylor series expansions of *P*, and *E*, about the western face *w* are required. These expansions are evaluated below,

$$T_P = T_w + \frac{\Delta x}{2}\frac{\partial T}{\partial x}\bigg|_w + \frac{1}{2}\left(\frac{\Delta x}{2}\right)^2 \frac{\partial^2 T}{\partial x^2}\bigg|_w + \frac{1}{6}\left(\frac{\Delta x}{2}\right)^3 \frac{\partial^3 T}{\partial x^3}\bigg|_w + \cdots \qquad (23)$$

$$T_E = T_w + \frac{3\,\Delta x}{2}\frac{\partial T}{\partial x}\bigg|_w + \frac{1}{2}\left(\frac{3\,\Delta x}{2}\right)^2 \frac{\partial^2 T}{\partial x^2}\bigg|_w + \frac{1}{6}\left(\frac{3\,\Delta x}{2}\right)^3 \frac{\partial^3 T}{\partial x^3}\bigg|_w + \cdots \qquad (24)$$

After multiplying equation (23) by 9, and subtracting equation (24) from the resultant equation, the following expression is obtained,

$$9\,T_P - T_E = 8\,T_w + 3\,\Delta x \frac{\partial T}{\partial x}\bigg|_w - \frac{3}{8}(\Delta x)^3 \frac{\partial^3 T}{\partial x^3}\bigg|_w + \cdots$$

Which upon rearrangement gives,

$$\frac{\partial T}{\partial x}\bigg|_w = \frac{9\,T_P - T_E - 8\,T_w}{3\,\Delta x} + O(\Delta x)^2 \qquad (25)$$

In equation (25) $O(\Delta x)^2$ represents the order of accuracy, which is 2. T_w in equation (25) can now be replaced by the specified value of temperature at the domain boundary, i.e. T_L. The resultant relation is substituted in equation (13), to replace the temperature gradient at face *w*.

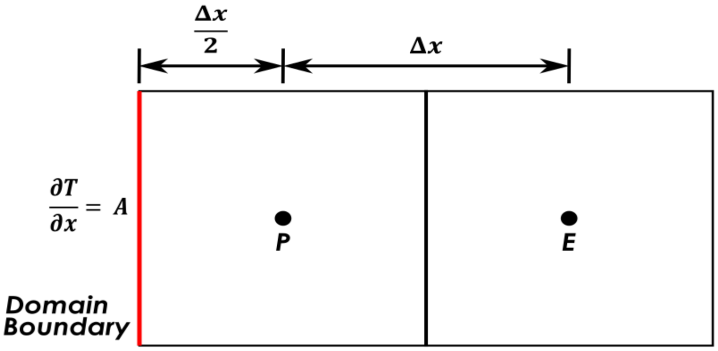

Fig. 2.4. Illustration of the Neumann boundary condition.

2.3.2.2 The Neumann boundary condition

The Neumann boundary condition is illustrated in *Fig. 2.4*, where ***A*** is an arbitrary constant. It can be applied directly, by substituting the value of the gradient in equation (13).

2.3.2.3 The Robin boundary condition

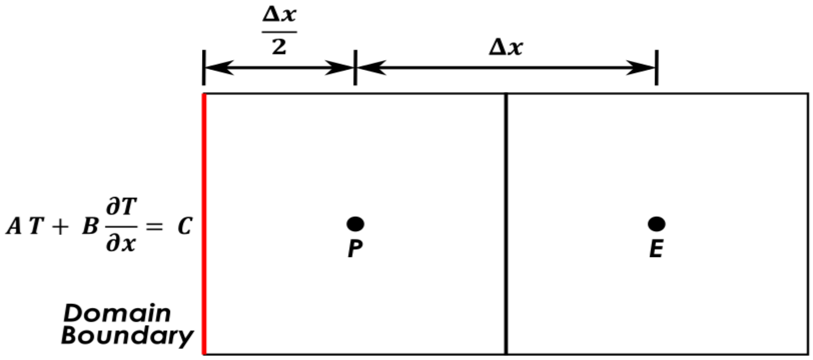

Fig. 2.5. Illustration of the Robin boundary condition.

Application of the Robin boundary condition, as illustrated in *Fig. 2.5* where ***A***, ***B***, and ***C*** are arbitrary constants, first requires its rearrangement, as,

$$T = \frac{C}{A} - \frac{B}{A}\frac{\partial T}{\partial x}\bigg|_w \tag{26}$$

T_w in equations (23), and (24), is now replaced by the relation on right side of equation (26), which gives the relations,

$$\begin{aligned} T_P &= \left(\frac{C}{A} - \frac{B}{A}\frac{\partial T}{\partial x}\bigg|_w\right) + \frac{\Delta x}{2}\frac{\partial T}{\partial x}\bigg|_w + \frac{1}{2}\left(\frac{\Delta x}{2}\right)^2 \frac{\partial^2 T}{\partial x^2}\bigg|_w \\ &+ \frac{1}{6}\left(\frac{\Delta x}{2}\right)^3 \frac{\partial^3 T}{\partial x^3}\bigg|_w + \cdots \end{aligned} \tag{27}$$

$$\begin{aligned} T_E &= \left(\frac{C}{A} - \frac{B}{A}\frac{\partial T}{\partial x}\bigg|_w\right) + \frac{3\,\Delta x}{2}\frac{\partial T}{\partial x}\bigg|_w + \frac{1}{2}\left(\frac{3\,\Delta x}{2}\right)^2 \frac{\partial^2 T}{\partial x^2}\bigg|_w \\ &+ \frac{1}{6}\left(\frac{3\,\Delta x}{2}\right)^3 \frac{\partial^3 T}{\partial x^3}\bigg|_w + \cdots \end{aligned} \tag{28}$$

After multiplying equation (27) by 9, and subtracting equation (28) from the resultant equation, the following relation is obtained,

$$9\,T_P - T_E = \frac{8\,C}{A} + \left(3\,\Delta x - \frac{8\,B}{A}\right)\frac{\partial T}{\partial x}\bigg|_w - \frac{3}{8}\,(\Delta x)^3 \frac{\partial^3 T}{\partial x^3}\bigg|_w + \cdots \tag{29}$$

Equation (29) upon rearrangement gives,

$$\left.\frac{\partial T}{\partial x}\right|_w = \frac{9\,T_P - T_E - \frac{8C}{A}}{\left(3\,\Delta x - \frac{8\,B}{A}\right)} + O(\Delta x)^2 \tag{30}$$

The relation on right side of (30) can now be substituted in equation (13), to replace the temperature gradient at face *w*.

2.4 Nonuniform distribution of MNPs

As stated in literature [13], the MNPs after intratumoral injection do not follow a uniform spatial distribution pattern, instead they follow a spatial distribution pattern that is similar to Gaussian distribution. This means that MNPs get distributed in the form of a sphere, with most of them settling at the injection site, and in its vicinity. In order to mimic this behavior of MNP spatial distribution, the relation given below is used [24],

$$g(x,y,z) = \frac{1}{\sqrt{(2\pi)^3}\sigma_x\sigma_y\sigma_z}\,exp\left\{-\frac{1}{2}\left[\left(\frac{x-\overline{x}}{\sigma_x}\right)^2 + \left(\frac{y-\overline{y}}{\sigma_y}\right)^2 + \left(\frac{z-\overline{z}}{\sigma_z}\right)^2\right]\right\} \tag{31}$$

Where, g represents the distribution function, σ_x, σ_y, and σ_z represent the standard deviations, and $\overline{x}$, $\overline{y}$, $\overline{z}$ the mean values, along the x, y, and z directions.

In this study, equation (31) is utilized to distribute the MNP mass. It is numerically integrated over each control volume using the 4-point Gaussian quadrature numerical integration method. This aids in evaluation of the MNP mass being distributed in each control volume.

Chapter 3

Comparative Study

In order to affirm the applicability of FVM for analysis of hyperthermia, a comparative study is performed in this chapter. The work presented by ***H. Zhang*** [15] is analyzed using FVM, and results are presented in the following sections.

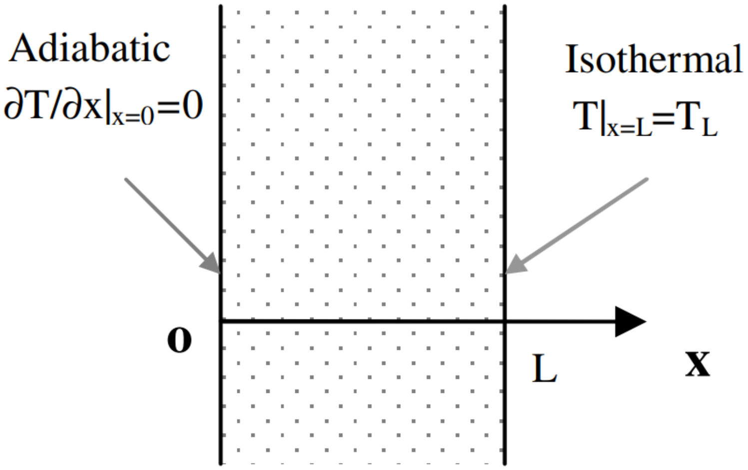

Fig. 3.1. One dimensional model, as presented by ***H. Zhang*** [15].

3.1 One dimensional model

Zhang [15] has used LBM in his work to analyze hyperthermia in one-dimensional and two-dimensional models. *Fig. 3.1*, shows the one-dimensional model of a tissue. Its left boundary is considered as adiabatic, whereas its right boundary is considered to be at a constant temperature of T_L. L is taken as 0.04 (m). The values of parameters considered to analyze this model are given in TABLE I.

TABLE I. Values of parameters considered in analysis of the one-dimensional model.

Parameter	***Value***	***Parameter***	***Value***
k_t	0.5 (W.m^{-1}.K^{-1})	ρ	1052 (kg.m^{-3})
ρ_b	1052 (kg.m^{-3})	c_p	3800 (J.kg^{-1}.K^{-1})
c_{pb}	3800 (J.kg^{-1}.K^{-1})	η_b	1×10^{-4} (s^{-1})

Q_m	400 (W.m^{-3})	T_a	37 (^{o}C)

3.1.1 Boundary Conditions

At *x=0*, temperature is specified with the aid of Neumann boundary condition, as,

$$\left.\frac{\partial T}{\partial x}\right|_{x=0} = 0$$

At *x=L*, temperature is specified with the aid of Dirichlet boundary condition, as,

$$T|_{x=L} = T_L = 30\ ^oC$$

3.1.2 Steady state analysis

A gird independence test is initially performed for the steady state case of the one-dimensional model. The numerical results of temperature distribution along the length of the model are plotted along with the analytical result in *Fig.3.2*.

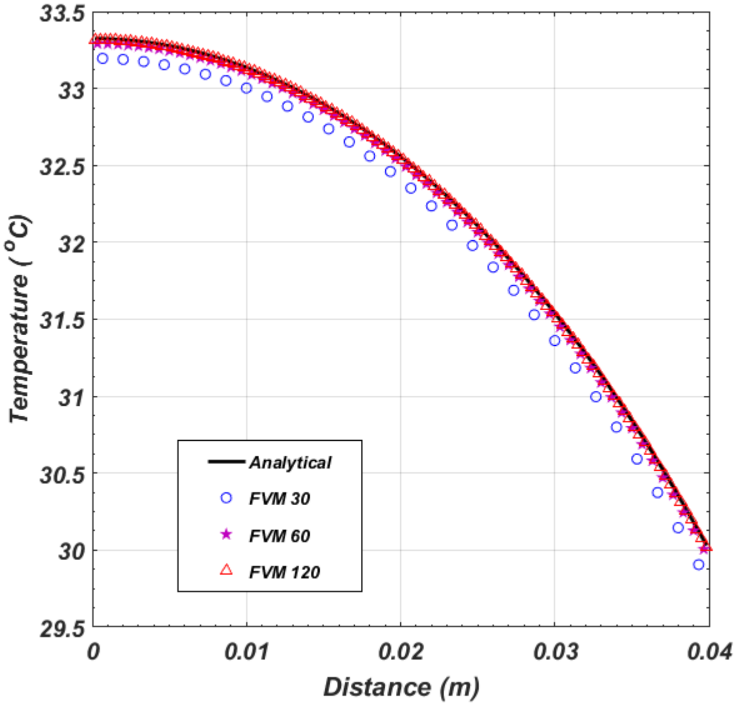

Fig.3.2. Grid independence test for one-dimensional model.

The relations for analytical solution are given below,

$$T(x) \quad = \quad T_e + (T_L - T_e)\frac{exp(\gamma x) + exp(-\gamma x)}{exp(\gamma L) + exp(-\gamma L)}$$

Where,

$$\gamma = \left(\eta_b \rho_b c_{pb}/k\right)^{1/2}, \qquad T_e = T_a + \frac{Q_m + Q_s}{\eta_b \rho_b c_{pb}}$$

The numerical results are plotted for 30, 60, and 120 finite volumes. It is seen that with 30 finite volumes, the numerical result does not completely agree with the analytical result. As the finite volumes are increased from 30 to 60, it is seen that the numerical result approaches the analytical result. As the finite volumes are increased to 120, it is seen that the difference between the numerical, and analytical results becomes negligible.

Finite volumes along with their respective root mean square error (RMSE) values for the steady state case of the one-dimensional model, are plotted in *Fig. 3.3*.

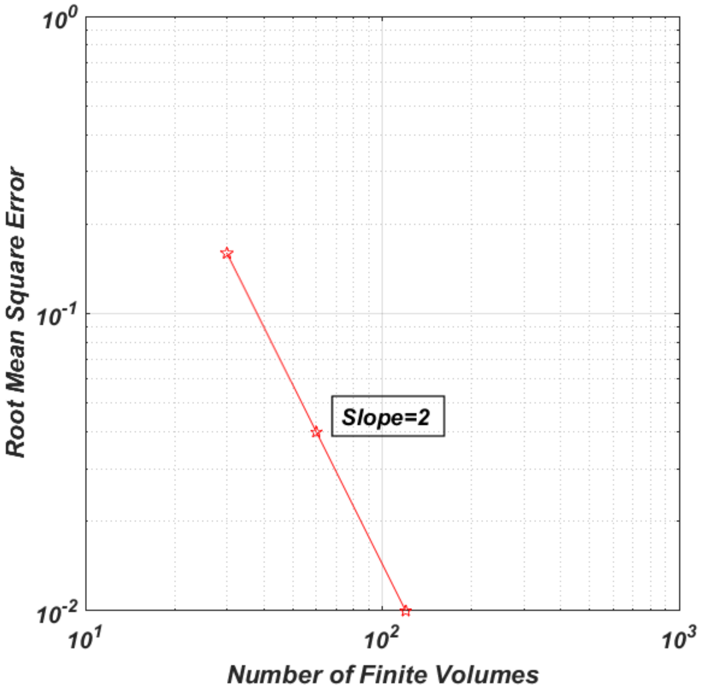

Fig. 3.3. A plot of RMSE v/s number of finite volumes, illustrating the order of accuracy of the scheme.

The slope of this plot indicates that the order of accuracy of the applied finite volume scheme is 2. This means that as the number of finite volumes is doubled, the respective RMSE becomes one-fourth. TABLE II shows the respective values used for this plot.

TABLE II. RMSE variation corresponding to the number of finite volumes.

Number of finite volumes	***RMSE***

30	0.1592
60	0.0398
120	0.0100

3.1.3 Time dependent analysis

For the time dependent case of the one-dimensional model, an initial condition is utilized. According to this condition, the model is initially at a temperature T_e. The relations for analytical solution for time dependent analysis are given as,

$$T(x,t) \quad = \quad T_e + \frac{2\alpha}{L}(T_L - T_e)\sum_{m=1}^{\infty}(-1)^{m-1}\beta_m cos(\beta_m x)\frac{1 - exp\left[-\left(\alpha{\beta_m}^2 + \eta^*\right)t\right]}{\alpha{\beta_m}^2 + \eta^*}$$

Where,

$$\alpha = \frac{k}{\rho c_p}, \qquad \beta_m = (m - 0.5)\frac{\pi}{L}, \qquad \eta^* = \eta_b\frac{\left(\rho_b c_{pb}\right)}{\rho c_p}$$

The numerical results, along with the analytical results of temperature distribution along

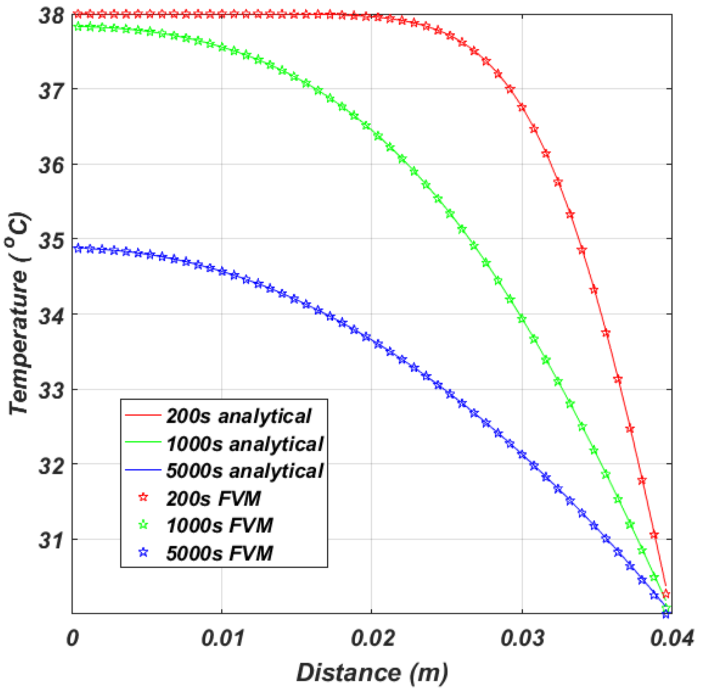

Fig.3.4. Plots of temperature distribution along the length of the model, comparing the numerical and analytical results, after 200s, 1000s, and 5000s.

the length of the model are plotted in *Fig.3.4*.

The plots illustrate temperature distribution along the length of the model after 200s, 1000s, and 5000s. The numerical results are in good agreement with analytical results. These plots reveal the heat sink effect of the blood. With increase in time from 200s to 1000s, and then to 5000s, a decrease of about 3°C in temperature at the left boundary is seen, as the heat is carried away by the blood.

3.2 Two-dimensional model

The two-dimensional model considered by ***H. Zhang*** [15], is shown in *Fig. 3.5*. The model consists of a square tumor at center, surrounded by a rectangular domain of healthy tissues. The tumor has sides of span $L/4$. Length and width of the outer domain are $2L$ and L, respectively. L is taken as 0.05 m.

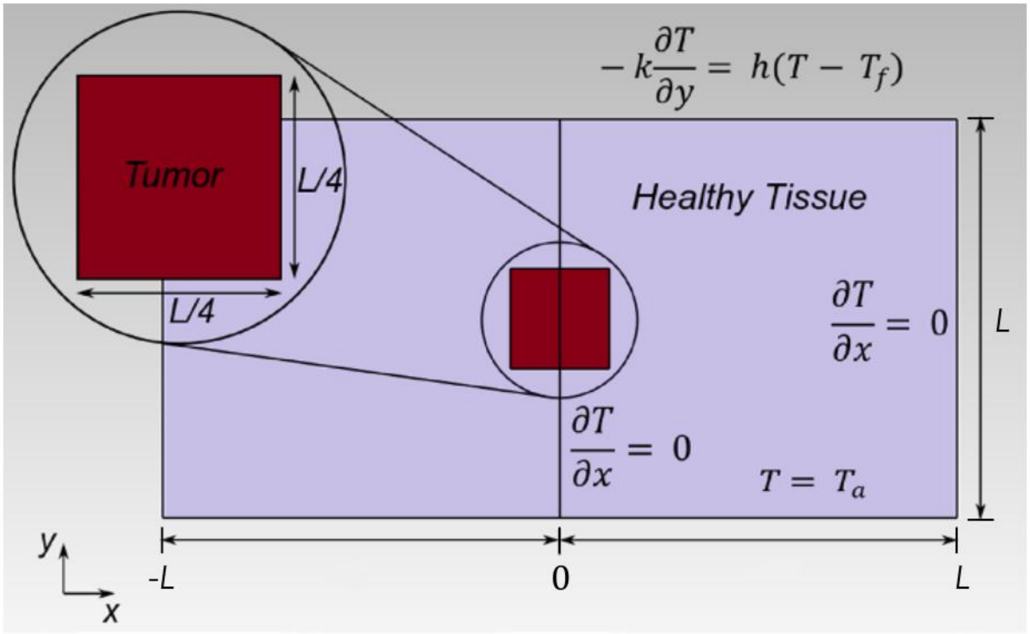

Fig. 3.5. Two-dimensional model, as presented by ***H. Zhang*** [15].

Just like the one-dimensional model, steady state, as well as time dependent analyses are performed for it. In this model, effects of blood perfusion rate, and metabolic heat generation rate of tumor are illustrated. Therefore, except for the blood perfusion rate and the metabolic heat generation rate of the tumor, all other parameters considered to analyze the model are same as those of the one-dimensional model. Two cases of blood perfusion rate and metabolic heat generation rate, are analyzed for this model. They are described below,

(a) Case I

In case *I*, the blood perfusion rate is taken as 1×10^{-3} (s^{-1}), and the metabolic heat generation rate is taken as 4000 ($W.m^{-3}$).

(b) Case II

In case *II*, the blood perfusion rate is taken as 1×10^{-2} (s^{-1}), and the metabolic heat generation rate is taken as 40,000 ($W.m^{-3}$).

3.2.1 *Boundary Conditions*

At $x=0$, the model is symmetric about y-axis, therefore the temperature at all points along the y-axis, at $x=0$, is specified with the aid of Neumann boundary condition, as,

$$\left.\frac{\partial T}{\partial x}\right|_{x=0} = 0$$

The boundary at $x=L$ is considered to be adiabatic, therefore the temperature here is specified with the aid of Neumann boundary condition, as,

$$\left.\frac{\partial T}{\partial x}\right|_{x=L} = 0$$

Lower surface of the model, at $y=0$, is assumed to be at a constant temperature of 37°C, and is therefore specified with the aid of Dirichlet boundary condition, as,

$$T|_{y=0} = 37\ {}^{o}C$$

Top surface of the model, at $y=L$ is assumed to be losing heat to the surroundings, therefore the temperature here is specified with the aid of Robin boundary condition,

$$-k\left.\frac{\partial T}{\partial y}\right|_{y=L} = h(T-T_f)$$

Where, h is the convective heat transfer coefficient and is taken as 20 ($W.m^{-2}.K^{-1}$), and T_f is taken as 20°C.

3.2.2 *Steady state analysis*

The plots of temperatures at $(x=0,\ y)$, and $(x,\ y=L)$, are shown in *Fig. 3.6* and *Fig. 3.7*. Temperature distribution for the two cases of blood perfusion rate, and metabolic heat generation rate of tumor is plotted in these figures. Temperature distribution for a third case in which the study domain is devoid of tumor is also plotted in these figures for comparison. From these plots it is observable that the metabolic heat generation rate of a tumor has a significant effect on temperature distribution within it, and its surrounding healthy tissues. Even though blood perfusion rate is increased in case *II*, but it cannot compensate for the increase in the metabolic heat generation rate of the tumor.

It is observable from the plots that the results obtained using FVM, agree well with those reported in literature using LBM, and the finite element method (FEM).

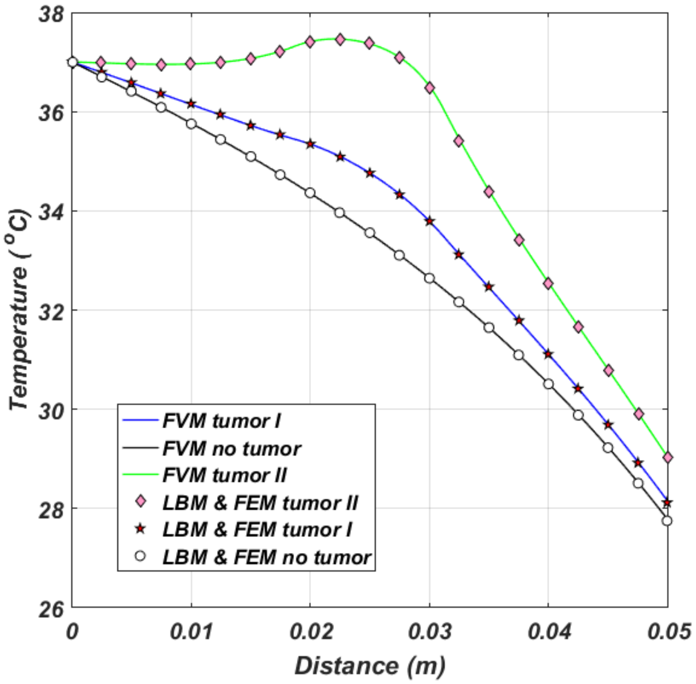

Fig. 3.6. Temperature plots at x=0, y, for steady state analysis.

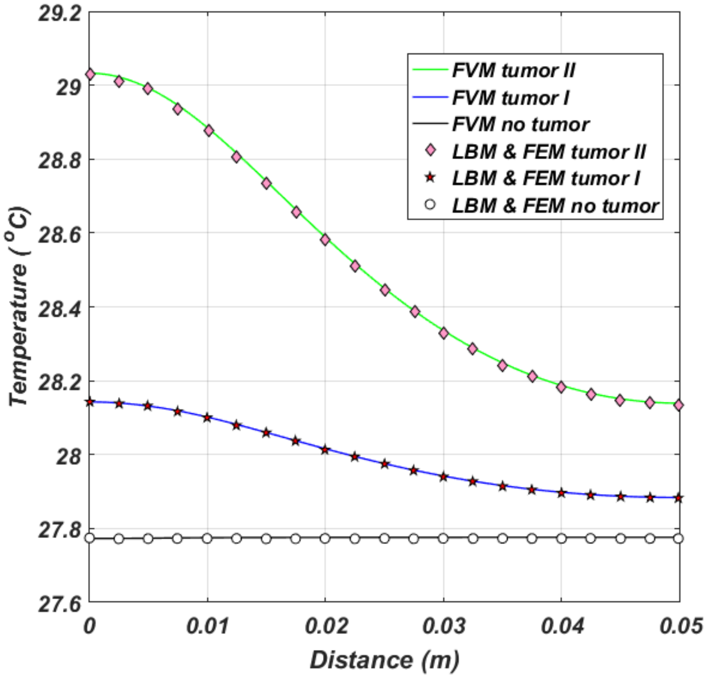

Fig. 3.7. Temperature plots at x, y=L, for steady state analysis.

3.2.3 *Time dependent analysis*

For the time dependent analysis, the blood perfusion rate, and metabolic heat generation rate, of the tumor are taken as 1×10^{-3} (s^{-1}), and 4000 (W.m^{-3}), respectively. Temperature distribution for case *I* is taken as the initial condition for time dependent analysis.

A time dependent heat source within the tumor, 100×t (W.m^{-3}), is also assumed in this analysis. Plots of temperature at *x=0, y*, at time 0s, 900s, and 1800s, are shown in *Fig. 3.8*. It is seen that, with increase time, heat generation within the tumor also increases, which causes the tumor temperature to also increase.

It is observable from the temperature plots that the results obtained using FVM, agree well with those obtained using LBM and FEM.

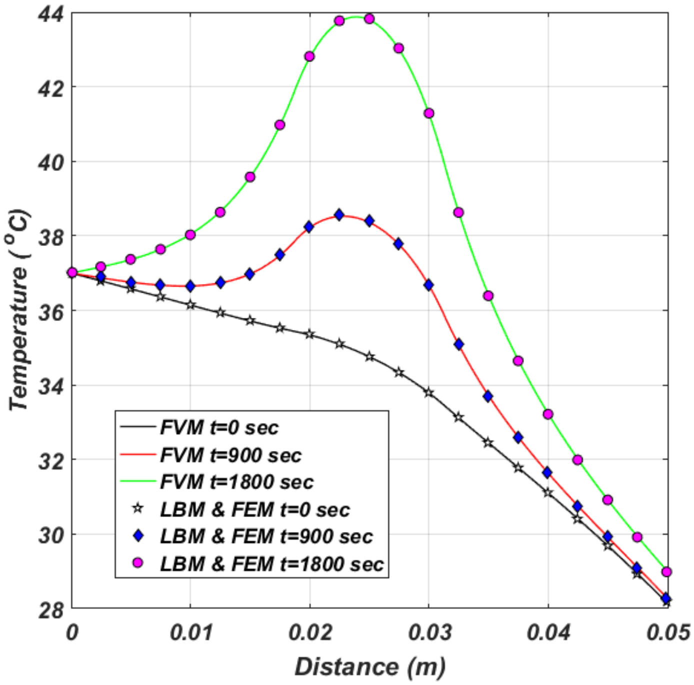

Fig. 3.8. Temperature plots at x=0, y, for time dependent analysis.

Chapter 4

Results and discussion

A three-dimensional version of the two-dimensional model analyzed chapter 3, is used to evaluate the differences in temperature distribution, when MNPs are distributed uniformly and nonuniformly, and treatment parameters are also varied. The geometric model on which the analysis is carried out is shown in *Fig. 4.1*. Due to symmetry, only right half of it is considered for analysis.

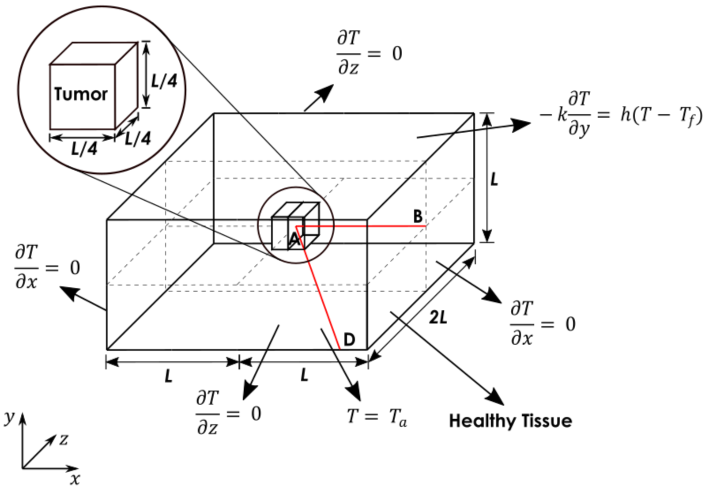

Fig. 4.1. Three-dimensional model considered for analysis.

Temperature distribution is evaluated along lines AB, and AD, as they pass through the most critical locations of the tumor. For uniform MNP distribution, MNPs are assumed to be homogenously distributed within the tumor. For nonuniform MNP distribution, two cases are analyzed, viz., single point MNP injection (injection at tumor center), and multi point MNP injection (injection at sites additional to tumor center). These cases of MNP spatial distribution are illustrated in *Fig. 4.2*. An elaborated view of the tumor along with injection locations of MNPs for the case of multi-point injection, is shown in *Fig. 4.3*.

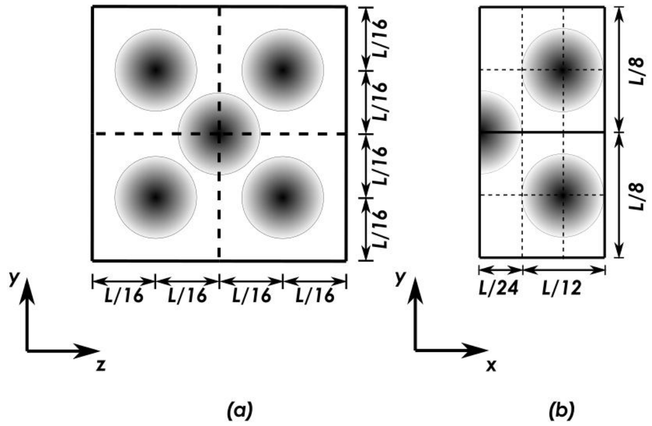

Fig. 4.3. Locations of injection sites for the case of multi-point injection: (a) The tumor when viewed along x-axis; (b) The tumor when viewed along z-axis.

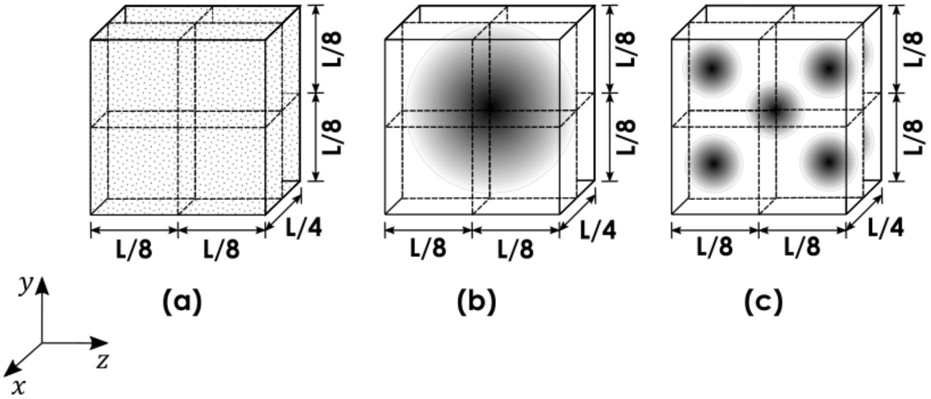

Fig. 4.2. MNP spatial distribution patterns considered for analysis: (a) Uniform MNP distribution; (b) Nonuniform MNP distribution: MNP injection at single site, i.e. tumor center; (c) Nonuniform MNP distribution: MNP injection at multiple sites, i.e. at sites additional to the tumor center.

A grid independent test presented in the following section affirms the accuracy of the numerical solution. In subsequent sections, the effects of treatment parameters, viz. amplitude and frequency of the AMF, and MNP dosage are illustrated. The properties of magnetite MNPs used for analysis are given in TABLE III, [18].

TABLE III. Properties of magnetite MNPs used in analysis.

$\boldsymbol{M_d}$ *(kA.m^{-1})*	***K*** *(kJ.m^{-3})*	$\boldsymbol{c_p}$ *(J.kg^{-1}.K^{-1})*	! *(kg.m^{-3})*
446	9	670	5180

4.1 Grid independence test

A grid independence test is performed to check the accuracy of numerically evaluated temperature distribution. This is done by evaluating the percentage change in values of temperature at specific locations within the study domain. With each increment in grid size, the temperatures obtained after the increment are compared with those before it. The change is evaluated with respect to the values obtained after the increment in grid size, as they are more accurate. The relation for percentage change evaluation is given as,

$$Percentage\ change \quad = \sqrt{\frac{\sum_{i=1}^{n}\left(\frac{T_i^{new} - T_i^{old}}{T_i^{new}}\right)_i^2}{n}} \times 100$$

Here, n denotes the number of locations at which the temperature values are considered for comparison. The temperature values for comparison are taken at distances of 0.0028 m, 0.0054 m, 0.0079 m, and 0.0105 m, from A, along the line AD. The different grids considered for the test, along with the respective percentage changes are given in TABLE IV.

TABLE IV. Grid size along with the respective percentage change.

Grid size	***Percentage change***
72×72×144	-
104×104×208	0.3323 %
136×136×272	0.1686 %
168×168×336	0.1022 %

As the percentage change in temperature values for the grid size 168×168×336 is below 5%, it can be said that the solution has become grid independent.

4.2 Effects of AMF amplitude on temperature distribution

In this section, the effects of variation in amplitude of the AMF on temperature distribution are presented. The MNP dosage and frequency of the AMF are taken as, 5 mg of magnetite / cm^3 of the tumor, and 100 kHz, respectively. ***Atkinson et al.*** 0, presented a plot of tolerability threshold of frequency and amplitude of the AMF, for the upper torso, *Fig. 4.4*. Based on this plot, three different values of AMF amplitude were considered for analysis, viz., $\mathbf{A_1}$ (5 kA.m^{-1}), $\mathbf{A_2}$ (7.5 kA.m^{-1}), and $\mathbf{A_3}$ (10 kA.m^{-1}). $\mathbf{A_1}$ lies right on the threshold limit, whereas $\mathbf{A_2}$ and $\mathbf{A_3}$ lie in the discomfort zone.

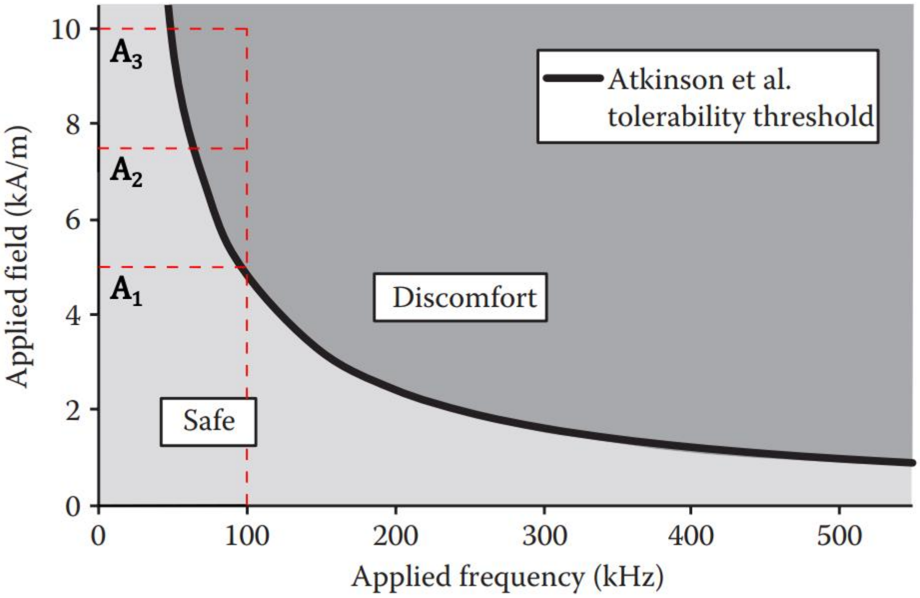

Fig. 4.4. Plot of frequency and amplitude tolerability threshold, presented by ***Atkinson et al.*** *0.The amplitude values considered for analysis,* $\mathbf{A_1}$ *(5 kA.m*$^{-1}$*),* $\mathbf{A_2}$ *(7.5 kA.m*$^{-1}$*), and* $\mathbf{A_3}$ *(10 kA.m*$^{-1}$*), are also illustrated.*

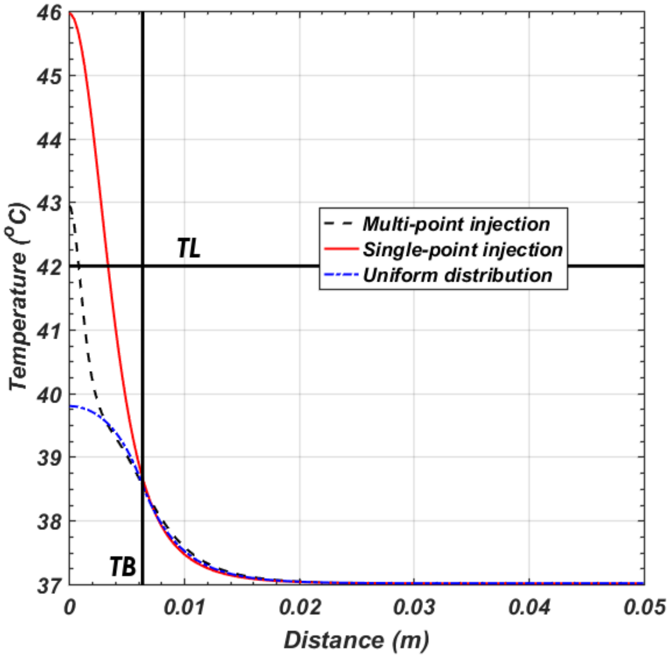

Fig. 4.5. Temperature distribution along AB, for all MNP spatial distribution patterns, for AMF amplitude $\mathbf{A_1}$ *(5 kA.m*$^{-1}$*), at 600s. TL and TB indicate, therapeutic limit, and tumor boundary.*

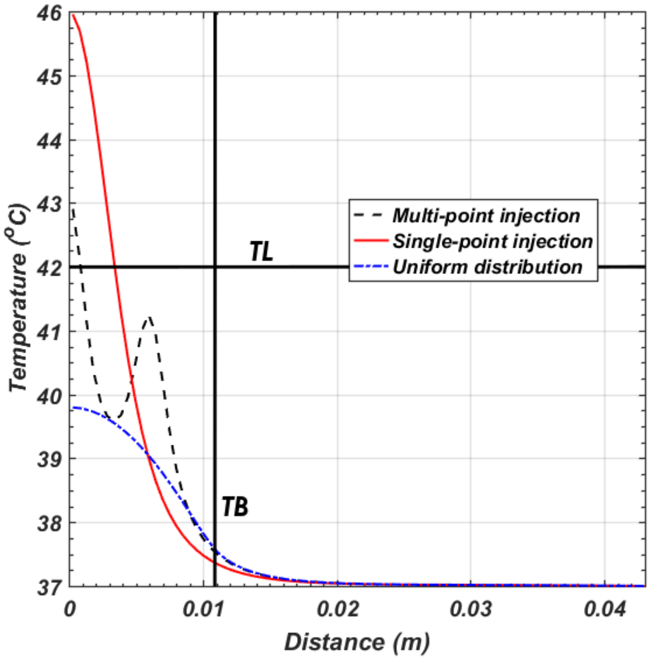

Fig. 4.6. Temperature distribution along AD, for all MNP spatial distribution patterns, for AMF amplitude $\mathbf{A_1}$ *(5 kA.m*$^{-1}$*), at 600s.*

(a) Case I: When amplitude is A_1

Plots of temperature distribution along AB, comparing uniform and nonuniform (single-point, and multi-point) MNP spatial distribution patterns, when amplitude is taken as $\boldsymbol{A_1}$ (5 kA.m^{-1}), are shown in *Fig. 4.5*. From the plot it is observable that only with nonuniform MNP spatial distribution, temperatures above the therapeutic limit are attainable. The tumor center temperature with single point and multi point injections reaches 46^{o}C, and 43^{o}C, respectively. For uniform MNP spatial distribution, the temperature at tumor center barely reaches 40^{o}C. It is also observable that along AB, single point injection is able to keep a greater extent of the tumor above the therapeutic limit.

Plots of temperature distribution, along AD, are shown in *Fig. 4.6*. The temperature distributions along AD of uniform MNP spatial distribution, and single point injection are similar to what were observed along AB in *Fig. 4.5*. For multi-point injection, a secondary peak after the initial dip in temperature along AD is observed. This rise in temperature is due to the presence of MNPs at sites additional to the tumor center. Even though the secondary peak of rise in temperature of multi point injection is below the therapeutic limit, but it offers a more uniform temperature distribution, in comparison to single point injection.

(b) Case II: When amplitude is A_2

For the second case the amplitude is increased from $\mathbf{A_1}$ (5 kA/m) to $\mathbf{A_2}$ (7.5 kA/m). The frequency of applied AMF, and MNP dosage are kept same as they were in ***Case I***, 100 kHz, and 5 mg of magnetite/ cm^3 of the tumor, respectively.

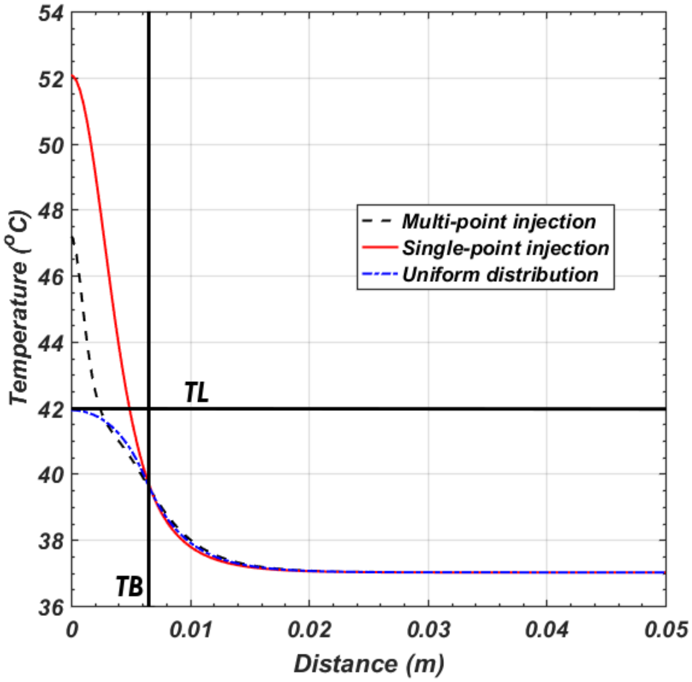

Fig. 4.7. Temperature distribution along AB, for all MNP spatial distribution patterns, for AMF amplitude $\mathbf{A_2}$ (7.5 kA.m^{-1}), at 600s.

The plots in *Fig. 4.7* illustrate temperature distribution along AB when amplitude is $\boldsymbol{A_2}$ (7.5 kA.m^{-1}). The increase in peak temperatures for all MNP spatial distribution cases, an effect of increase in the AMF amplitude, is observable in the plots. The peak temperatures for single-point and multi-point injection have incremented by 6^{o}C, and 4^{o}C, whereas for uniform distribution of MNPs, this increment is of about 2^{o}C. From this it is evident that the greater the MNP mass injected at a specific location, greater is the variation in temperature at that location, when treatment parameters are varied. The peak temperature of single-point injection, 52^{o}C exceeds the range of temperatures used in hyperthermia (42^{o}C-47^{o}C). Such high temperatures lead to thermal ablation, which is avoided or kept minimum during hyperthermia treatment. Single-point injection is still able to keep a greater extent of the tumor above the therapeutic limit, in comparison to multi-point injection, along AB. With uniform MNP distribution only the temperature at tumor center reaches the therapeutic limit, whereas rest of the tumor remains below it. Therefore, with current treatment parameters hyperthermia is be ineffective with uniform MNP distribution.

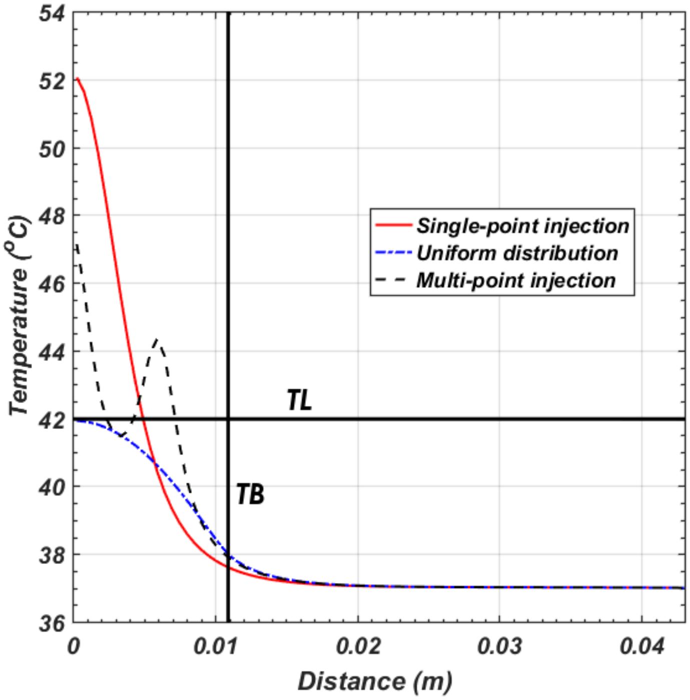

Fig. 4.8. Temperature distribution along AD, for all MNP spatial distribution patterns, for AMF amplitude $\boldsymbol{A_2}$ *(7.5 kA.m*$^{-1}$*), at 600s.*

The plots in *Fig. 4.8* illustrate the temperature distribution along AD for AMF amplitude $\boldsymbol{A_2}$ (7.5 kA.m^{-1}). It is seen that with single-point injection the temperature for complete tumor cannot be kept above the therapeutic limit. Also, the distance up to which therapeutic limit is observable along AD, is shorter for single point injection, in contrast to multi-point injection. This is due to the additional injection sites near tumor periphery, and the increased amplitude.

Multi-point injection proves to be very efficient and effective with the current treatment parameters.

(c) Case III: When amplitude is A_3

In this case the AMF amplitude is further increased to $\boldsymbol{A_3}$, while keeping the frequency and MNP dosage constant.

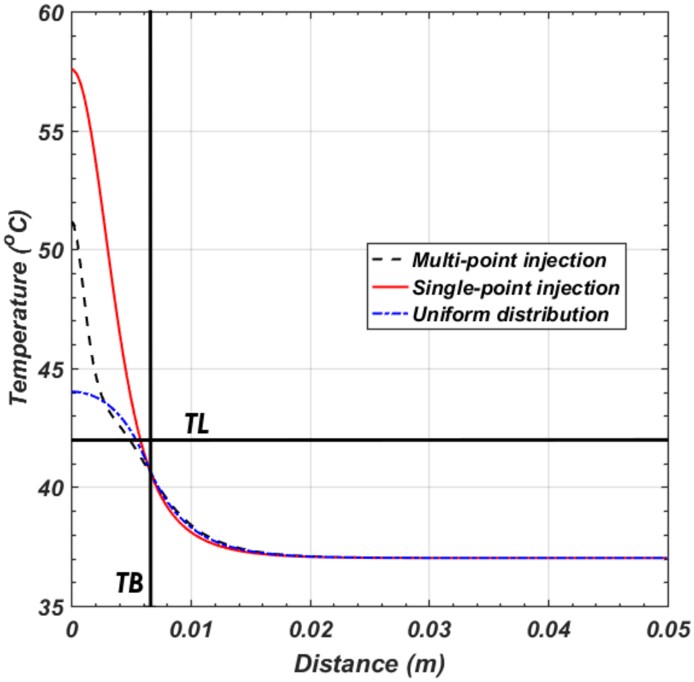

Fig. 4.9. Temperature distribution along AB, for all MNP spatial distribution patterns, for AMF amplitude $\boldsymbol{A_3}$ *(10 kA.m^{-1}), at 600s.*

Fig. 4.9 shows the plots of temperature distribution along AB, when the AMF amplitude is $\boldsymbol{A_3}$ (10 kA.m^{-1}). With increase in AMF amplitude the values of temperature at tumor center increase further. For single-point and multi-point injection tumor center temperatures reach 57.5^{o}C, and 51^{o}C, after incrementing by 5.5^{o}C, and 4^{o}C, respectively. For uniform MNP distribution tumor center temperature increments by 2^{o}C and reaches 44^{o}C. With high AMF amplitude ($\boldsymbol{A_3}$), the temperatures at tumor center for both, single-point and multi-point injection cases exceed the range of treatment temperatures. It is observable that with the current choice of amplitude, all three MNP spatial distribution cases are able to keep the complete tumor along AB above the therapeutic limit.

Fig. 4.10 compares the temperature distributions along AD, when AMF amplitude $\boldsymbol{A_3}$ is used. It is observable from the figure that the region in which the temperature exceeds treatment temperature range, is smaller for multi-point injection. This is because the spread of MNPs at each injection site in multi-point injection is smaller in comparison to the spread in single point injection. Therefore, an increment in treatment parameters above the safe range, is more

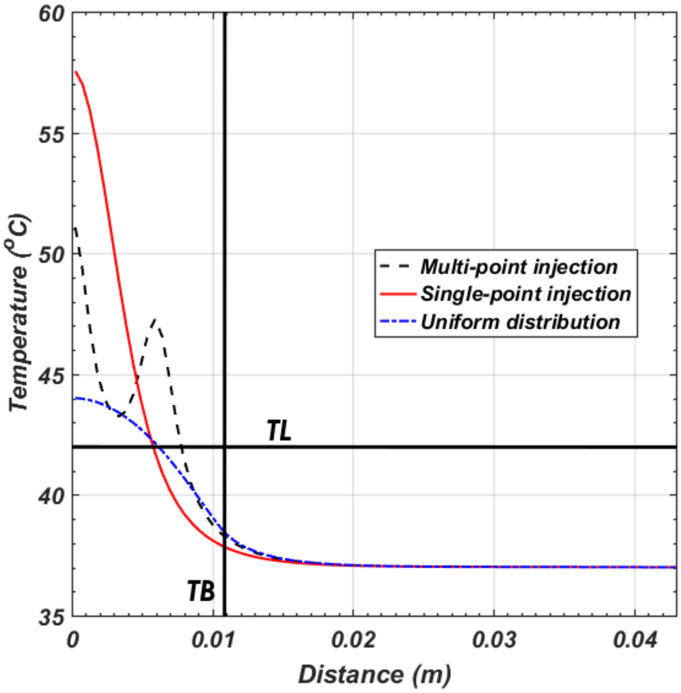

Fig. 4.10. Temperature distribution along AD, for all MNP spatial distribution patterns, for AMF amplitude $\boldsymbol{A_3}$ *(10 kA.m*$^{-1}$*), at 600s.*

dangerous for the patient when MNPs are injected at a single point within the tumor. Also, with multi-point injection a greater distance along AD is kept above the therapeutic limit.

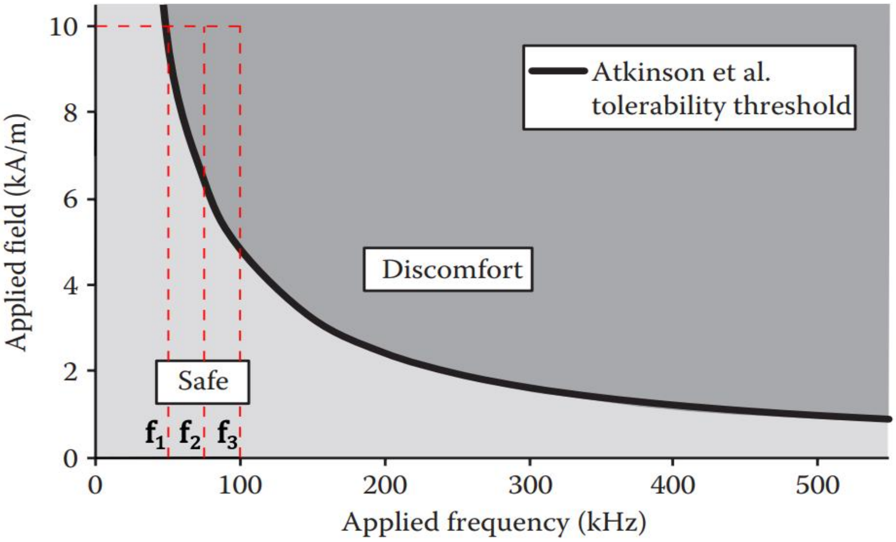

*Fig. 4.11. AMF frequency values, **f_1** (50 kHz), **f_2** (75 kHz), and **f_3** (100 kHz), considered for analysis are illustrated in the threshold plot presented by* **Atkinson et al.** *0.*

4.3 Effects of AMF frequency on temperature distribution

Effects of variation in AMF frequency are presented in this section. The AMF frequency is varied, while keeping the MNP dose, and AMF amplitude constant. The values of AMF frequency were selected from the threshold plot given by ***Atkinson et al.*** 0. 5 mg of Magnetite/cm^3 of the tumor, and 10 kA.m^{-1}, are used as the respective MNP dose, and AMF amplitude for the analysis. Three different values of AMF frequency, f_1 (50 kHz), f_2 (75 kHz), and f_3 (100 kHz), as shown in *Fig. 4.11*, are used, and the results are presented in the following subsections.

(a) Case I: When frequency is f_1

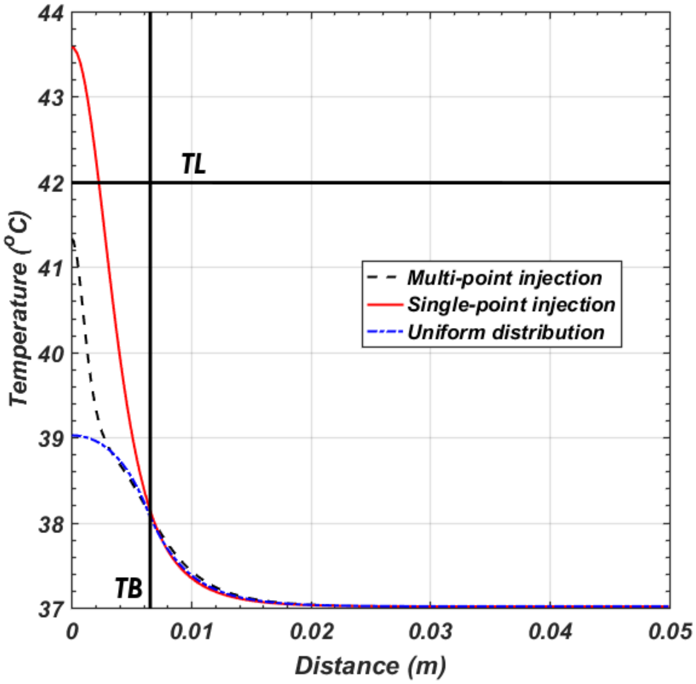

Fig. 4.12. Temperature distribution along AB, for all MNP spatial distribution patterns, for AMF frequency $\boldsymbol{f_1}$ *(50 kHz), at 600s.*

Fig. 4.12 illustrates the temperature distribution along AB for all three MNP spatial distribution cases, when AMF frequency $\boldsymbol{f_1}$ (50 kHz) is used.

With frequency $\boldsymbol{f_1}$, only single-point injection is able to raise the temperature of tumor center above the therapeutic limit, 43.6^{o}C. With multi-point injection and uniform MNP distribution, tumor center attains temperatures of only 41.3^{o}C, and 39^{o}C. The temperature at tumor boundary for all three cases is same, 38.2^{o}C.

Temperature distribution along AD for ***Case I***, for all MNP spatial distribution patterns is illustrated in *Fig. 4.13*. The trends that curves of temperature distribution follow along AD are similar to those observed in previous analysis. Both multi-point injection, and uniform MNP distribution, turn out to be ineffective with the current choice of treatment parameters. Single-point injection too turns out to be inefficient as it raises the temperature of only the tumor center and a small region in its vicinity above the therapeutic limit, thus leaving the rest of the tumor below it.

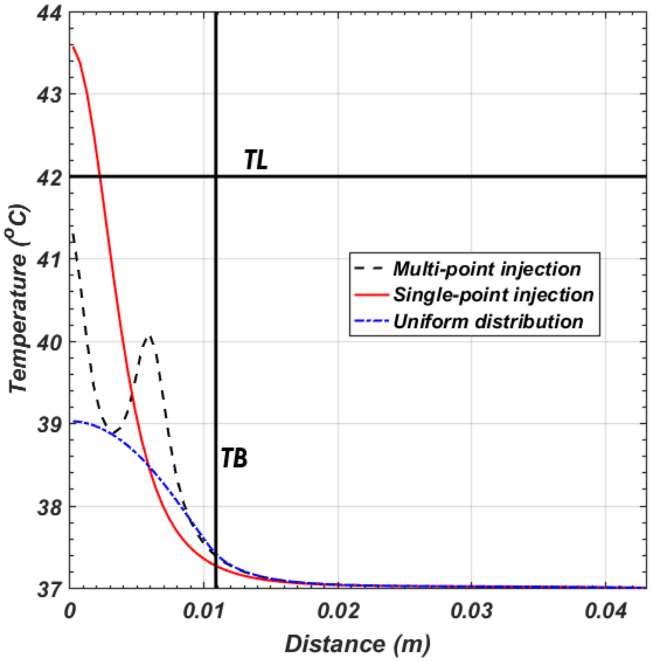

Fig. 4.13. Temperature distribution along AD, for all MNP spatial distribution patterns, for AMF frequency ***f_1*** *(50 kHz), at 600s.*

(b) Case II: When frequency is f_2

Fig. 4.14 illustrates the temperature distribution along AB, when AMF frequency f_2 (75 kHz) is considered. The increment in frequency from f_1 (50 kHz) to f_2 (75 kHz) results in increment of tumor center temperatures of all three cases of MNP spatial distribution patterns under analysis. The tumor center temperature increments by 6.1°C with single-point injection, 4.6°C with multi-point injection, and 1.4°C with uniform distribution. This behavior of temperature increments is similar to what was observed in cases of AMF amplitude increments.. The tumor center reaches 50.1°C with single-point injection, 46°C with multi-point injection, and 41.3°C with uniform MNP distribution. It is observable from the plots that only single-point injection and multi-point injection exceed the therapeutic limit. With single point injection, a greater distance along AB is kept above the therapeutic limit, as compared to multi-point injection, but the temperatures at tumor center and in its vicinity exceed the range of treatment temperatures. Exceeding the range of treatment temperatures will lead to thermal ablation. Therefore, single point injection proves to be inefficient with the current choice of treatment parameters. With uniform MNP distribution, the tumor remains completely below the therapeutic limit, therefore it turns out ineffective with the current choice of treatment parameters.

Plots of temperature distribution along AD are illustrated in *Fig. 4.15*. The trends of temperature distribution, of single point injection and uniform MNP distribution in *Fig. 4.15*, are

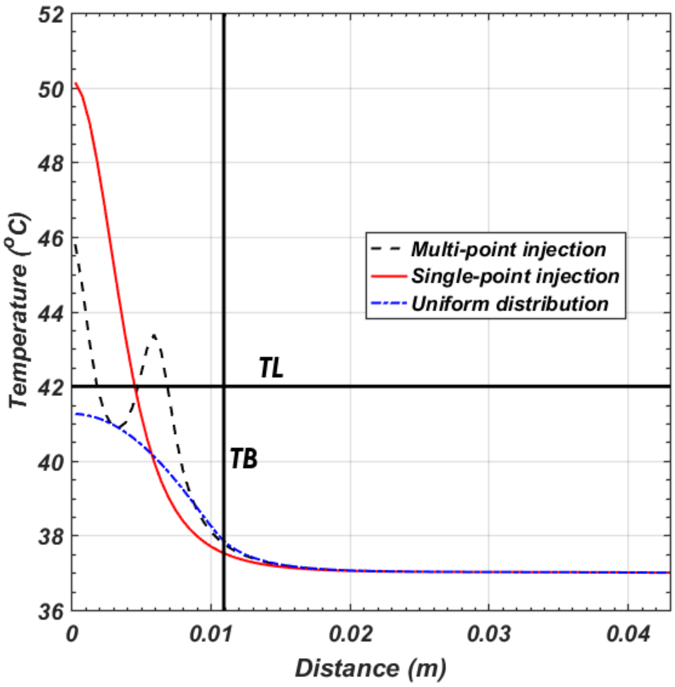

Fig. 4.15. Temperature distribution along AD, for all MNP spatial distribution patterns, for AMF frequency f_2 (75 kHz), at 600s.

frequency f_2 (75 kHz), at 600s.

similar to what were observed in *Fig. 4.14*. The increment in temperature at the center of secondary injection site of multi-point injection along AD is of 3.5^{o}C, the value of which with ***f*$_1$** was 40^{o}C, and in the present case it is 43.5^{o}C. This increment is less than what is observed at tumor center with multi-point injection. This is because the secondary injection site is located very close to the healthy tissues which are at a temperature that is lower than that of the tumor. Multi-point injection keeps the temperature at tumor center within the range of treatment temperatures and compared to single point injection it also keeps a greater extent of the tumor above the therapeutic limit. Therefore, multi-point injection with the current choice of treatment parameters proves to be effective as well as efficient.

(c) *Case III: When frequency is f$_3$*

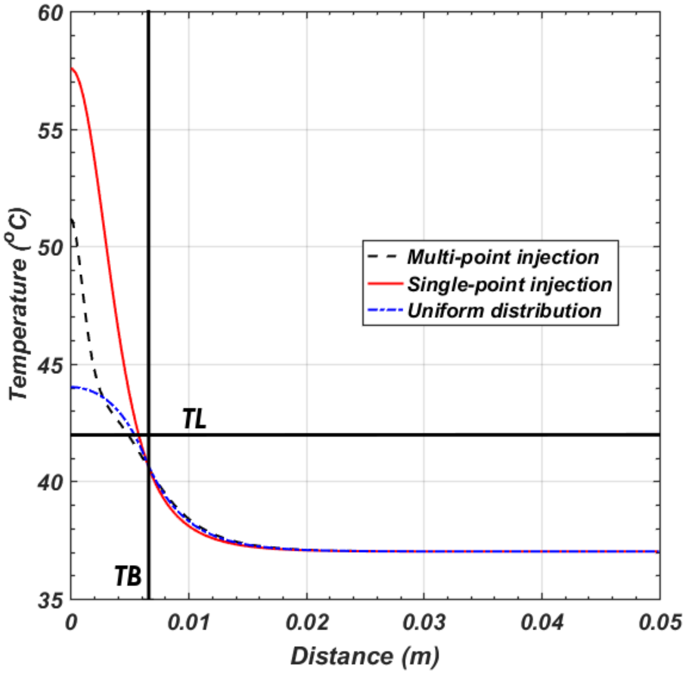

*Fig. 4.16. Temperature distribution along AB, for all MNP spatial distribution patterns, for AMF frequency **f**$_3$ (100 kHz), at 600s.*

Fig. 4.16 illustrates the plots of temperature distribution along AB of all cases of MNP spatial distribution patterns, when the AMF frequency is ***f*$_3$** (100 kHz). Tumor center temperature with single-point injection increments by 7.4^{o}C after the increase in AMF frequency from ***f*$_2$** to ***f*$_3$**. These increments for multi-point injection, and uniform MNP distribution are of 5^{o}C, and 2.7^{o}C. The temperature increments at tumor center for the present case, are greater than what were observed when the AMF frequency was increased from ***f*$_1$** to ***f*$_2$**. Also, the magnitude of increments of tumor center temperature did not increase for all cases of MNP spatial distribution patterns when AMF amplitude was increased from ***A*$_2$** to ***A*$_3$**, compared to when it was increased from ***A*$_1$** to ***A*$_2$**. The increment for single-point injection had decreased, while that of multi-point injection and uniform MNP distribution remained same. The observations of increase in AMF frequency from f_2 to f_3 also reveal an increase in increment magnitude compared to what was observed when frequency was increased from ***f1*** to f_2.

With current treatment parameters, all three cases of MNP spatial distribution patterns are able to keep the tumor completely above the therapeutic limit, but multi-point and single point injection exceed the range of treatment temperatures, which makes them inefficient for the current case of analysis.

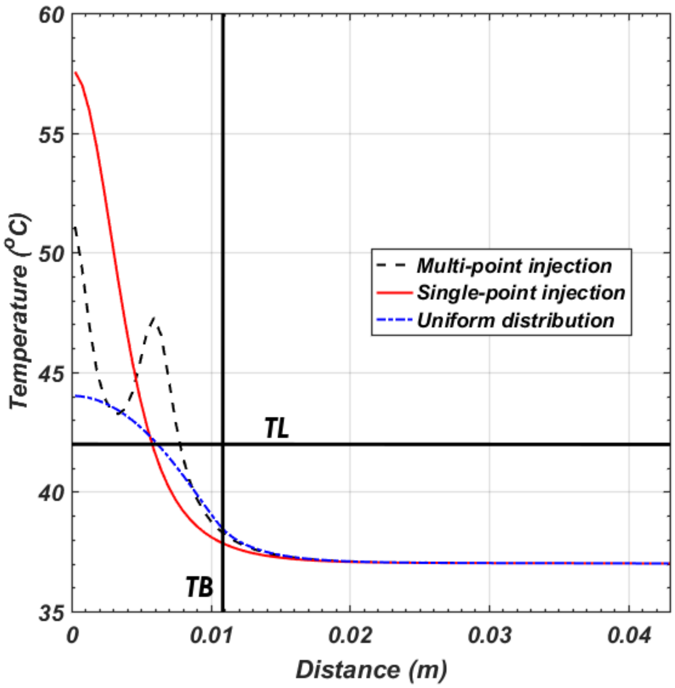

Fig. 4.17. Temperature distribution along AD, for all MNP spatial distribution patterns, for AMF frequency f_3 *(100 kHz), at 600s.*

The plots of temperature distribution along AD, of all MNP spatial distribution cases, are illustrated in *Fig. 4.17*. It is observable from the plots that only with multi-point injection can a greater extent of the tumor be kept above the therapeutic limit, in comparison to single-point and multi-point injection. This plot also illustrates that the temperature of secondary peak of multi-point injection has incremented by 4^{o}C, reaching 47^{o}C.

As both single-point and multi-point injection cases exceed the range of treatment temperatures, and uniform MNP distribution is unable to keep the complete tumor above the therapeutic limit, none of the MNP spatial distribution cases prove to be effective or efficient.

4.4 Effects of MNP dose on temperature distribution

As observed in the previous sections, only multi-point injection proved to be the most efficient and effective MNP spatial distribution pattern. It was also observed that multi-point injection gave the best results when AMF frequency and amplitude were taken as f_2 (75 kHz) and

$\boldsymbol{A_2}$ (7.5 kA.m^{-1}). The combination of $\boldsymbol{A_2}$ and $\boldsymbol{f_2}$ also lies very close to the safe limit in the threshold plot presented by ***Atkinson et al.*** 0, which makes them highly favorable treatment parameters, *Fig. 4.18*. Therefore, the analysis of effects of MNP dose on temperature distribution is carried out only for multi-point injection, at AMF frequency and amplitude of ***f₂*** (75 kHz) and

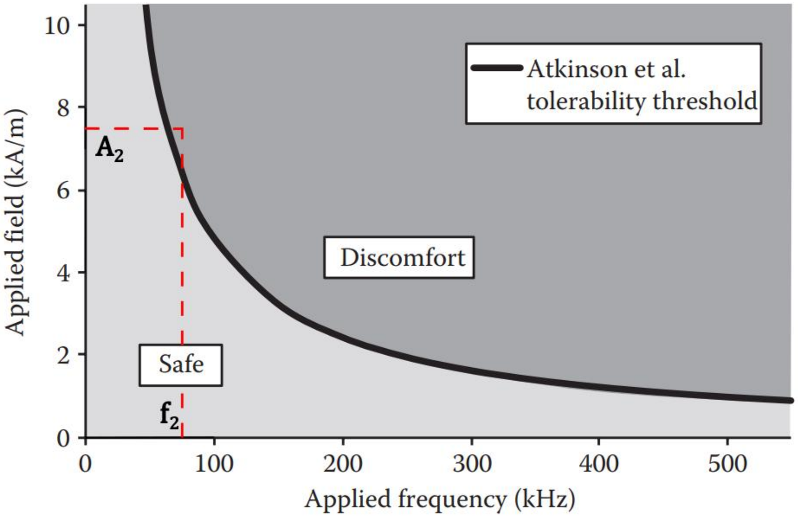

Fig. 4.18. AMF amplitude and frequency used to analyze the effects of MNP dose on temperature distribution is illustrated on the threshold plot given by ***Atkinson et al.*** *0.*

A₂ (7.5 kA.m^{-1}). The typical dose of magnetite MNPs that is used in experimental studies of hyperthermia is 5 mg of magnetite / cm^3 of the tumor. In this section the effects of incrementing and decrementing the MNP dose on temperature distribution, are illustrated. Similar to the

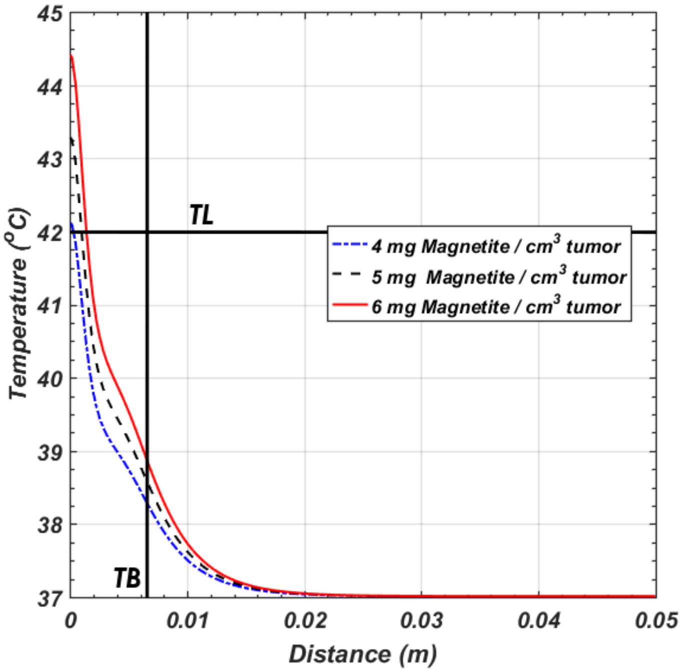

Fig. 4.19. Temperature distribution along AB, for all MNP doses considered, at AMF frequency ***f₂*** *(75 kHz), and amplitude* ***A₂*** *(7.5 kA.m^{-1}).*

results presented in prior sections, temperature distributions along AB, and AD with decreased, typical, and increased MNP dose, are plotted for the case of multi-point injection. The MNP doses considered for analysis are 4 mg of magnetite / cm^3 of the tumor, 5 mg of magnetite / cm^3 of the tumor, and 6 mg of magnetite / cm^3 of the tumor.

Fig. 4.19 illustrates the temperature distribution along AB, for all MNP doses considered. It is observed that with 4 mg of magnetite the temperature at tumor center just crosses the therapeutic limit, whereas with 5 and 6 mgs of MNPs tumor center reaches 43.25^{o}C, and 44.375^{o}C. It is observable that the effect of variation in MNP dose is not as pronounced as was observed in cases of frequency and amplitude. Also, the distance from tumor center along AB up to which the tumor is above the therapeutic limit, is very small. This is because all the secondary injection sites are distant from AB. A very subtle effect of the presence of secondary injection sites is observed near the tumor boundary.

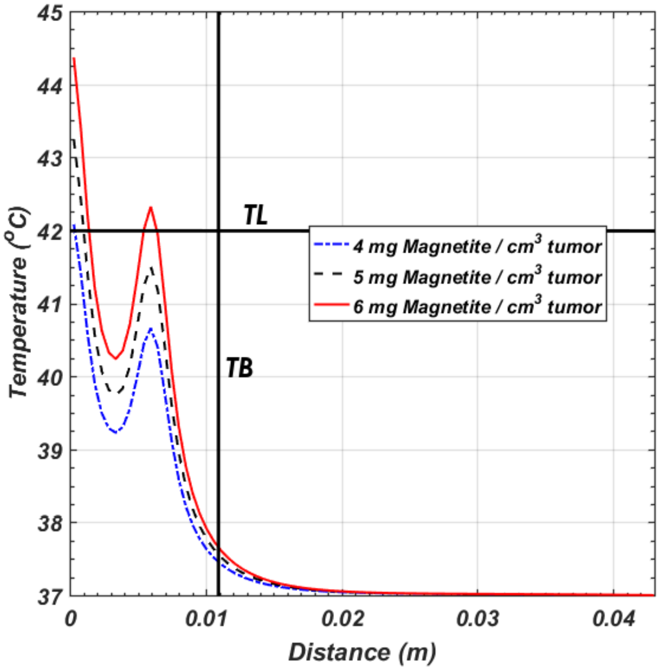

Fig. 4.20. Temperature distribution along AD, for all MNP doses considered, at AMF frequency ***f*₂** *(75 kHz), and amplitude* ***A*₂** *(7.5 kA.m^{-1}).*

Fig. 4.20 illustrates the temperature plots along AD, of all cases of MNP doses considered. The presence of secondary injection sites is observable in this figure. As the effects of MNP dose variation are not very pronounced, the differences between the temperature values at the secondary peaks are also minor. The secondary peaks with 4 mg, 5 mg, and 6mg, reach 40.75^{o}C, 41.5^{o}C, and 42.25^{o}C. Only with 6mg of magnetite the secondary peak exceeds the therapeutic limit. Therefore, it can be said that with AMF frequency and amplitude very close to the safe limit, a slightly higher dose of MNPs is required for the treatment to be effective and efficient, but it should be kept in mind that very high doses of MNPs may prove to be toxic for the patient.

Chapter 5

Conclusions

In this study the treatment parameters of MNP induced hyperthermia that strongly affect its outcomes, are numerically analyzed. The numerical analysis involved utilization of FVM. Special attention was paid to the spatial distribution patterns of MNPs that are injected intratumorally. Uniform (ideal case) and nonuniform (single-point and multi-point injection) distribution of MNPs are considered in the analysis for comparison. Nonuniform spatial distribution of MNPs is modelled using the Gaussian distribution. It is observed that multi-point injection offers a more uniform temperature distribution. Presence of MNPs at and in the vicinity of multiple injection sites aids in keeping most of the tumor above the therapeutic limit. Effects of variation in AMF frequency and amplitude are observed to be more pronounced, than those of variation in MNP dose. Efficiency and efficacy of multi-point MNP injection depends on the choice of treatment parameters (MNP dose, and AMF frequency and amplitude), and the spread of MNPs within the tumor after injection. Also, the injection sites that are located closer to the tumor periphery may require a higher dose of MNPs in order to compensate for the loss of heat to the nearby healthy tissues that are at lower temperatures than those observed within the tumor. It was observed that if a greater dose of MNPs is injected intratumorally, the variation in temperature with variation in AMF frequency and amplitude, will also be great. Utilization of AMF frequency and amplitude close to the safe limit in the tolerability threshold presented by ***Atkinson et al.*** 0 may not always give temperatures greater than the therapeutic limit, therefore higher MNP doses may be required. It should also be kept in mind that higher doses lead to higher toxicity. Increase of treatment parameters beyond certain limits may lead to induction heating within the healthy tissues, therefore the parameters for the treatment should be carefully chosen.

5.1 Scope for future work

1. Effects of number of injection sites on temperature distribution can be studied. Increasing the number of injection sites may result in uniform temperature distribution.
2. The spread of MNPs in multi-point injection sites will vary depending on the mass of MNPs injected. Greater mass of MNPs can be injected closer to the tumor periphery, while keeping the mass of MNPs injected near the tumor center small, in order to obtain an approximation of uniform temperature distribution.

3. When AMF frequency and amplitude are increased beyond certain values, the tissues may heat up due to induction, this will lead to heating of unwanted areas. Relations associated with induction heating can also be utilized in order to make the analysis more realistic.

4. Not all tumors are located away from the blood vessels. Therefore, other mathematical models that consider blood flow through the tissues can also be utilized to make the study more realistic.

5. The current study assumes that all injected MNPs are of the same diameter. Variation of MNP diameter can also be considered in future studies.

6. Blood perfusion through the tissues is also assumed to be constant in this study. Relations for temperature dependent blood perfusion can be adopted in future studies.

7. Thermal damage and survival fraction, based on temperature within the tumor can be evaluated to better assess the treatment.

8. Tumors generally are of arbitrary shapes, therefore to analyze a realistic geometry finite volume method with unstructured grids along with other numerical methods can be used.

9. The current study is just a theoretical assessment of MNP induced hyperthermia. Experimental studies are still required to affirm its validity.

References

[1] World Health Organization 2018, accessed 1 June 2018, www.who.int/news-room/fact-sheets/detail/cancer

[2] Cancer Research UK 2017, accessed 2 June 2018, www.cancerresearchuk.org/about-cancer/what-is-cancer/why-some-cancers-come-back#why

[3] The American Society of Clinical Oncology 2018, accessed 2 June 2018, https://www.cancer.net/survivorship/long-term-side-effects-cancer-treatment

[4] P. Gas, “Essential Facts on the history of Electromedicine,” *Prz. Elektrotech.*, vol. 87, 2011, pp. 37-40.

[5] Fehleisen, “Die Aetiologie des Erysipels,” 3.

[6] W. B. Coley, “Contribution to the knowledge *Ann. Surg.*, vol. 14, 1891, pp. 199-220.

[7] D.K. Chatterjee, P. Diagaradjane, and S. Kr -mediated hyperthermia in cancer therapy,” *Ther. Deliv.*, vol. 2, 2011, pp. 1001-1014.

[8] Magforce AG, accessed 5 June 2018, www.magforce.de/home.html

[9] L. H. Reddy, J. L. Arias, J. Nicolas, and P Characterization, Toxicity and Biocompatibility, Pharmaceutical and Biomedical Applications,” *Chem. Rev.*, vol. 112, 2012, pp. 5818-5878.

[10] A. E. Deatsch and B. A. Evans, “Heating efficiency in magnetic *J. Magn. Magn.*, vol. 354, 2014, pp. 163-172.

[11] I. Hilger et al., “Electromagnetic heating vitro and in vivo studies in human cadavers ogy, vol. 218, 2001, pp. 570-575.

[12] M. Johannsen et al., “Thermotherapy using m radiation in an orthotopic rat model of p *The Prostate*, vol. 66, 2006, pp. 97-104.

[13] M. Salloum, R. H. Ma, D. Weeks, and L. Zhu, “Controlling nano magnetic nanoparticle hyperthermia for cancer treatment: experimental study in agarose gel,” *Int. J. Hyperthermia*, vol. 24, 2008, pp. 337-345.

[14] S. Maenosono, and S. Saita, “Theoretical ticles as heating a elements for magnetic hyperthermia,” *IEEE Trans. Magn.*, vol. 42, 2006, pp. 1638-1642.

[15] H. Zhang, “Lattice Boltzmann method for so *Phys. Med. Biol.*, vol. 53, 2008, pp. N15-N23.

[16] M. Salloum, R. Ma, and L. Zhu, “Enhanceme nanoparticle hyperthermia: optimization o *Int. J. Hyperthermia*, vol. 25, 2009, pp. 309-321.

[17] A. A. Golneshan, and M. Lahonian, "The eff nanoparticle dispersion on temperature distribution in a spherical tissue in magnetic fluid hyperthermia using the lattice Boltzmann method," *Int. J. Hyperthermia*, vol. 27, 2011, pp. 266-274.

[18] M. Lahonian, and A. A. Golneshan, "Numeric ture distribution in a spherical tissue in magnetic fluid hyperthe *IEEE Trans. Nanobioscience*, vol. 10, 2011, pp. 262-268.

[19] A. A. Golneshan, and M. Lahonian, "Diffusi -site injection process within a biological tissue during magnetic fluid hyperthermia using lattice Boltzmann method," *Mech. Res. Commun.*, vol. 38, 2011, pp. 425-430.

[20] M. Mital, and H. V. Tafreshi, "A methodolog magnetic nanoparticle hyperthermia treatment," *Int. J. Num. Meth. Biomed. Engng.*, vol. 28, 2012, pp. 205-213.

[21] S. Soni, H. Tyagi, R. A. Taylor, and A. Kur for thermal ablation of a tumor subjected to nanoparticle assisted thermal thera *J. Therm. Biol.*, vol. 43, 2014, pp. 70-80.

[22] I. Astefanoaei, I. Domitru-Stancu, and "Analysis in magnetic fluid hyperthermia," *Chinese Phys. B.*, vol. 23, 2014.

[23] K. Yue, C. Yu, Q. Lei, Y. Luo, and X. Zhan simulation of effect of vessel bifurcation on heat transfer in magneti *Appl. Therm. Eng.*, vol. 69, 2014, pp. 11-18.

[24] F. Soetaert, L. Dupré, R. Ivkov, and G. amplitude modulation for enhanced magnetic nanoparticle hyper *Biomed. Eng.-Biomed. Tech*, vol. 60, 2015, pp. 491-504.

[25] F. Soetaert, L. Dupré, and G. Crevecoeur, superparamagnetic nanoparticle properties on bioheat transfer in magnetic nanoparticle hyperthermia," *2016 International symposium on Fundamentals of Electrical Engineering (ISFEE)*, Bucharest, 2016, pp. 1-5.

[26] Y. Tang, T. Jin, and R. C. C Flesch, "Nu hyperthermia considering nanoparticle clus *IEEE Trans. Magn.*, vol. 53, 2017, pp. 1-6.

[27] H. H. Pennes, "Analysis ontthei srseuset ianrgt ehruimaln *J. Appl. Physiol.*, vol. 1, 1948, pp. 93-122.

[28] S. M. Becker, and A. V. Kuznetsov, Heat Transfer and Fluid Flow in Biological Processes, Academic Press, 2015.

[29] R. E. Rosensweig, "Heating magnetic fluid v *J. Magn. Magn. Mater.*, vol. 252, 2002, pp. 370-374.

[30] W. J. Minkowycz, E. M. Sparrow, J. P. Abraham, Nanoparticle Heat Transfer and Fluid Flow, vol. 4, CRC Press, 2013.

[31] S. Mazumder, Numerical Methods for Partial Differential Equations, Academic Press, 2015.

W. J. Atkinson, I. A. Brezovich, and D. P. Chakra
with Thermal Seeds," *IEEE Transactions on Biomedical Engineering*, vol. BME-31, 1984, pp. 70-75.